

Latitudinal- and Height- Dependent Long-Term Climatology of Propagating Quasi-16-day in the Troposphere and Stratosphere

Wentao Tang

Wuhan University <https://orcid.org/0000-0002-7831-9447>

Shao Dong ZHANG (✉ zsd@whu.edu.cn)

Wuhan University

Chun Ming HUANG

Wuhan University

Kai Ming HUANG

Wuhan University

Yun Gong

Wuhan University

Quan Gan

University of Colorado at Boulder: University of Colorado Boulder

[Full paper](#)

Keywords: quasi-16-day wave, long-term trend

Posted Date: June 9th, 2021

DOI: <https://doi.org/10.21203/rs.3.rs-577454/v1>

License:  This work is licensed under a Creative Commons Attribution 4.0 International License.

[Read Full License](#)

Latitudinal- and height- dependent long-term climatology of propagating quasi-16-day in the troposphere and stratosphere

Wen Tao TANG^{1, 2, 3} Shao Dong ZHANG*^{1, 2, 3} Chun Ming HUANG^{1, 2, 3} Kai Ming
HUANG^{1, 2, 3} Yun GONG^{1, 2, 3} Quan GAN⁴

¹School of Electronic Information, Wuhan University, Wuhan, China

² Key Laboratory of Geospace Environment and Geodesy, Ministry of Education, Wuhan, China

³State Key Laboratory of Information Engineering in Surveying, Mapping and Remote Sensing, Wuhan University, Wuhan, China

⁴Laboratory for Atmospheric and Space Physics, University of Colorado Boulder, Boulder, US

16 Corresponding author: Zhang Shaodong

17 Email Address: zsd@whu.edu.cn

21 Funding information: The National Natural Science Foundation of China (through grants
22 41874177 and 41874178)

23 **Abstract.** The global amplitude of the westward propagating quasi-16-day wave (16DW)
24 with wavenumber 1 (Q16W1), the strongest component of 16DW, is derived from European
25 Centre for Medium-Range Weather Forecasts ERA-Interim reanalysis temperature data set
26 from February 1979 to January 2018. The strong climatological mean amplitudes of the
27 Q16W1 appear in winter in the upper stratosphere at high latitudes in both hemispheres, and
28 the wave amplitude is stronger in the Northern Hemisphere (NH) than in the Southern
29 Hemisphere (SH). Multivariate linear regression is applied to calculate responses of the
30 Q16W1 amplitude to QBO (quasi-biennial oscillation), ENSO (El Niño-Southern Oscillation),
31 solar activity and the linear trend of the Q16W1 amplitude. The QBO signatures of the
32 Q16W1 amplitude are mainly located in the stratosphere. In addition to the significant QBO
33 response in the low latitude and low stratosphere, the largest QBO response occurs in the
34 region with the strongest Q16W1 climatology amplitude. There no significant responses to
35 ENSO and solar activity are observed. The linear trend of the monthly mean Q16W1
36 amplitude is generally positive, especially in the mid-high latitudes of the stratosphere. The
37 trend is asymmetric about the equator and significantly stronger in the NH than in the SH. The
38 trend shows obvious seasonal changes, that is, stronger in winter, weaker in spring and
39 autumn. Further investigation suggests that the background and local instability trends
40 contribute most of the increasing trend of the Q16W1 amplitude. In winter in both
41 hemispheres, the weakening trend of eastward zonal wind provide more favourable
42 background wind for Q16W1 upward propagation, in autumn and winter in the NH and in
43 spring, autumn and winter in the SH, the increasing trend of local instability may enhance the
44 wave excitation.

45 **Introduction**

46 Planetary waves (PWs), one of the main components of atmospheric waves, play a key
47 role in transporting energy, momentum and chemical species among different atmospheric
48 regions and are thus important in determining local and global atmospheric climatology and
49 transient structures (Tsuda et al. 1994). PWs are global-scale oscillations predominantly
50 generated by orography and diabatic heating caused by the distribution of land and sea in the
51 troposphere (quasi-stationary PWs) or by irregular thermal or mechanical forcing in the lower
52 atmosphere and/or by instabilities in the middle atmosphere (travelling PWs) with periods
53 near 2, 5, 10 and 16 days (Andrews et al. 1987; Huang et al. 2013). Under certain conditions,
54 PWs can propagate from the troposphere into the mesosphere and lower thermosphere (MLT),
55 and wavenumber 1 and wavenumber 2 components are usually the predominant components
56 (Charney and Drazin 1961).

57 The quasi 16-day wave (16DW) is one of the PWs and was identified as the second
58 symmetric westward propagating Rossby mode with zonal wavenumber 1 (Salby 1981a, b).
59 In the realistic atmosphere, due to Doppler shifting by the non-zero background flow, the
60 period of 16DWs is from 12 to 20 days (Amitava et al. 2016). The 16DWs have been
61 extensively reported over the past decades from ground-based measurements (Mitchell et al.
62 1999; Das et al. 2010), satellite-borne measurements (McDonald et al. 2011; Alexander and
63 Shepherd 2010) and reanalyses data sets (Vineeth et al. 2010). Combinations of ground-based
64 and satellite-based analyses are also used to reveal the characteristics of 16DWs (Meek and
65 Manson 2009). These findings show that 16DWs are prominent in the MLT from October to
66 April. However, the exploration of 16DWs is relatively insufficient in the lower atmosphere,

67 most likely due to the lack of high-quality data sets, i.e., data with a long duration, good
68 continuity, and high resolution. Since local observations cannot provide a global distribution,
69 and satellite observations with long-term duration usually are rare. Hence, global data with a
70 long duration are necessary for a further study.

71 Long-term variation is an important topic in atmospheric science. Previous
72 observational and modelling studies have shown some long-term trends in atmospheric
73 parameters, such as temperature (She et al. 2015) and wind fields (Kozubek et al. 2017).
74 These studies revealed some important changes in the atmosphere from the lower atmosphere
75 to the mesosphere. Hu and Tung (2002) determined that there were no obvious stratospheric
76 wavenumber 1 and wavenumber 2 PW activity trends in early and midwinter from November
77 to January during 1950–2000 at 200, 100, 50 and 20 hPa along the 60°N latitude circle.
78 However, a significant negative PW activity trend from January to February 1979–2000 at
79 100 hPa in the NH mid-high latitudes was revealed (Randel et al. 2002). Hu et al. (2019)
80 suggested that the trend for stratospheric wave intensity from 200 hPa to 10 hPa at NH
81 mid-high latitudes was strengthening during 1979–2000 and weakening during 2001–2015.
82 However, most of the studies are related to PW, research on travelling PW activity trends,
83 especially the Q16W1, is rare. Hence, the global trend in Q16W1 amplitude is far from being
84 fully understood.

85 The background wind can significantly affect the excitation, propagation and
86 dissipation of PWs. On the other hand, PWs will impact the background wind by depositing
87 energy and momentum into the background atmosphere through various dissipation processes.
88 Therefore, PWs might be related to the background wind at different time scales. Most

89 previous studies on the 16DW-mean flow interactions have focused on the dynamic process at
90 the time scale of the wave period (Huang et al. 2013), seasonal scale (Huang et al. 2017) and
91 intranasal variabilities (Espy et al. 1997; Day et al. 2011) rather than the climate scale. Thus,
92 to further understand the activity trend of 16DWs, we need more studies on 16DWs and their
93 links with the background wind at the climate time scale.

94 For the purpose of investigating the global-scale and long-term characteristics of
95 16DWs in the stratosphere and below, the ERA-Interim reanalysis datasets were applied in
96 our study. The responses to the quasi-biannual oscillation (QBO), El Niño-Southern
97 Oscillation (ENSO) and 11-year solar cycle (SC) and the linear trend of the strongest wave
98 mode of 16DW in the troposphere and the stratosphere during February 1979–January 2018
99 were examined. In addition, we attempt to find a possible link between the wave and
100 background wind and instability at the climate time scale. To this end, the rest of paper is
101 organized as follows. In the following section, we introduce the adopted data, the dominant
102 modes of the 16DW and the calculation method. Subsequently, the global climatology of
103 wave amplitude is presented. In sections 4 and 5, we present the latitude- and
104 height-dependent responses of the 16DW to the QBO and the linear trend of the strongest
105 wave mode of 16DW, respectively. In the last section, we provide a brief summary of our
106 analyses.

107 **2. Data description and analysis approach**

108 The global 6-hourly temperature and zonal wind data from the ERA-Interim dataset
109 were downloaded from the European Centre for Medium-Range Weather Forecasts (ECMWF)
110 for the period from February 1979 to January 2018 (39 years in total) at 37 pressure levels

111 from 1000 hPa to 1 hPa and utilized in this study (Kallberg et al., 2004). The ERA-Interim
112 uses cycle 31r2 of the ECMWF'S Integrated Forecast System, which was introduced
113 operationally in September 2006, with a reduced Gaussian grid with approximately 79 km
114 spacing from surface and other grid-point fields and a 60-level vertical resolution extending to
115 0.1 hPa. The vertical resolution of the temperature product decreases with altitude, with a
116 range of 0.1–1 km in the troposphere, which is reduced to 1–4.5 km in the stratosphere. For
117 each day, the temperatures are interpolated at four UTCs with a 6-hour interval: 0000 UTC,
118 0600 UTC, 1200 UTC and 1800 UTC. We chose the products on a grid of 72×143 points with
119 2.5° longitude and 2.5° latitude resolution.

120 At each pressure level, we first calculated the background temperature by a linear
121 fitting within a 60-day sliding window with a 1-day shift interval. Then, the temperature
122 disturbance could be obtained by subtracting the background temperature and zonal mean
123 temperature from the raw data. To demonstrate the dominant modes of 16DWs, we calculated
124 the frequency-wavenumber spectra by performing a two-dimensional fast Fourier transform
125 on the temperature disturbance in each sliding 60-day window at each height (Huang et al.
126 2013; Gong et al. 2019). Furthermore, at each height, all spectra at different days were
127 averaged to determine the temporal averaged spectra. Finally, a mean spectrum was obtained
128 by averaging the temporal averaged spectra at all pressure levels. The mean
129 frequency-wavenumber spectrum averaged from 38,475,745 spectra is shown in Figure 1,
130 which shows that the most prominent spectral peak has a period of 15 days and a wavenumber
131 of W1, with the largest amplitude of 0.46 K. The secondary wave mode with a period of 20
132 days and a wavenumber of E1 can also be recognized. Here, we focus only on the strongest

133 PW , i.e., 16DW with wavenumber W1, which is named as Q16W1 for simplicity.

134 To extract the monthly averaged amplitudes of Q16W1, in each sliding 60-day
135 window to determine the amplitude at the centre day of the window (Wu et al. 1995), we
136 employed a harmonic fitting to the temperature perturbations at each latitude bin and each
137 pressure level, according to Equation (1).

138

$$T' = B_j \cos[2\pi(t_i/p_j - s\lambda_i)] + C_j \sin[2\pi(t_i/p_j - s\lambda_i)] \quad (1)$$

139 T' is the time series of the temperature perturbation; p_j , t_i , λ_i are, respectively, the
140 jth wave period, ith time, and longitude; and $s = 1$ is the wavenumber. In each window, p_j
141 varies from 12 to 20 days with an interval of 0.25 days, which accord to 6-hourly data interval
142 in ECMWF. B_j and C_j are the two coefficients to be fitted for the jth period, and then the
143 wave amplitude T_j can be specified by $T_j = \sqrt{B_j^2 + C_j^2}$. In each 60-day window, we can
144 specify 33 wave amplitudes corresponding to 33 periods p_j in total, among which, the
145 maximum amplitude and the corresponding period are regarded as the Q16W1 amplitude and
146 period, at the centre day of the 60-day window, respectively. Finally, all Q16W1 amplitudes at
147 different centre days within each month were averaged to derive the monthly mean amplitude
148 of the Q16W1 amplitude, i.e., T_A .

149 Multivariate linear regression (MLR) analysis was extensively utilized to isolate
150 specific signals for zonal-mean anomalies in temperature, zonal wind, ozone, and gravity
151 wave energy from the simulation and observation data (Gan et al., 2017; Weber et al., 2018).
152 PWs could be modulated by QBO, ENSO and SC, which display as interannual variation in
153 PWs. There are also seasonal changes in PWs, which are mainly reflected in annual,
154 semi-annual, tri-annual and quarter-annual oscillations. Therefore, when performing MLR

155 analysis on the amplitude of the Q16W1, the influences from all these factors should be
156 considered. So, we chose a particular set of indices for the regression.

157 Before implementing MLR, some inflection point analysis based on the piecewise
158 fittings of the Q16W1 amplitude had been performed during the 39-year period, so
159 confirming that the linear trend fit over entire time range is appropriate. In this study, MLR
160 analysis was performed on the time series of the monthly mean amplitude of the Q16W1, i.e.,
161 $T_A(t)$. The fitting equation is written as:

$$162 T_A(t) = A + B \times t + C \times Solar(t) + D \times ENSO(t) + E \times QBO1(t) + F \times QBO2(t) + \\ 163 G_1 \times \cos(\omega t) + G_2 \times \sin(\omega t) + H_1 \times \cos(2\omega t) + H_2 \times \sin(2\omega t) + I_1 \times \\ 164 \cos(3\omega t) + I_2 \times \sin(3\omega t) + J_1 \times \cos(4\omega t) + J_2 \times \sin(4\omega t) \\ 165 (2)$$

166 where t is time in months (478 months over 39 years), $\omega = 2\pi/12$ months, and B is the
167 coefficient of the linear trend. The third to the fourteenth terms on the right side of Equation
168 (2) are the linear correlations between the $T_A(t)$ and the SC, ENSO, two QBO components,
169 annual oscillation (AO), semi-annual oscillation (SAO), tri-annual oscillation (TAO) and
170 fourth-annual oscillation (FAO), respectively, which are thought to be the dominant
171 contributors to the variations in Q16W1. Among them, the third to the sixth terms denote
172 the inter-annual variations in Q16W1; the seventh to the fourteenth terms are the intra-annual
173 variations in Q16W1. $G = \sqrt{G_1^2 + G_2^2}$, $H = \sqrt{H_1^2 + H_2^2}$, $I = \sqrt{I_1^2 + I_2^2}$ and $J = \sqrt{J_1^2 + J_2^2}$
174 represent the annual, semi-annual, tri-annual and fourth-annual oscillation components,
175 respectively. Here, the indices of $F_{10.7cm}$ (unit: sfu, $1\text{sfu} = 10^{-22} W m^{-2} Hz^{-1}$) and
176 multivariate ENSO index (MEI) (downloaded from <http://www.esrl.noaa.gov/psd/>), shown in

177 Figure 2a and 2b, respectively, are used as proxies of the SC and ENSO activities. The time
178 series QBO1 and QBO2, shown in Figure 2c are the two QBO components with a
179 quarter-cycle phase difference (Gan et al. 2017). These two QBO time series correspond to
180 the first two components of the empirical orthogonal functions (EOFs) extracted from the
181 equatorial stratospheric zonal winds at 5 different levels (70, 50, 30, 20, and 10 hPa)
182 measured by radiosonde over Singapore (downloaded from
183 <http://www.geo.fu-berlin.de/en/met/ag/strat/produkte/qbo/index.html>) (Wallace et al. 1993).

184 The delay autocorrelation coefficients of all independent variables, including SC,
185 ENSO, QBO1, QBO2, AO, SAO, TAO and FAO are calculated and all close to zero. The
186 delay cross-correlation coefficients between all variables are also obtained, except that the
187 correlation between the SOLAR and the ENSO index is 0.27, all others are lower than 0.20.
188 These small correlations indicate that they are all independent. Gan et al. [2017] have also
189 proved that multiple linear regression with these independent variables is a commonly used
190 credible algorithm (Gan et al. 2017). And, in the MLR calculation, the confidence levels of
191 the regression coefficients are estimated according to the variance-covariance matrix and
192 Student's t-test (Kutner et al. 2004).

193 **3. Global Q16W1 Climatology**

194 Figure 3 demonstrates the latitude-pressure distribution of the monthly mean Q16W1
195 amplitude averaged over 39 years. It is notable that the latitude-pressure distribution exhibits
196 a well-defined hemispheric symmetry for the similarity in increase with altitude. More
197 specifically, the maximal amplitudes occur at 2 hPa in both hemispheres, due to the
198 decreasing atmospheric mass density decreases with height. However, markable differences

199 also clearly appear in the latitudinal variations. Wave amplitudes in the NH are larger than in
200 the SH, with the maxim of 1.98 K (at 60°N, 2 hPa) for NH and 1.32 K (at 45°S, 2 hPa) for SH,
201 respectively, which are quantitatively consistent with the results in Gong et al. (2019).

202 The monthly zonal-mean Q16W1 amplitudes at six latitudes, representing high,
203 middle, and low latitudes in two hemispheres, are shown in Figure 4. At 65°N/S, the AO of
204 the Q16W1 amplitude is dominant in the whole stratosphere (100–1 hPa), with peak
205 amplitude appearing in winter months, and the amplitude is larger in the NH than in the SH.
206 For instance, the maximum amplitude in the NH is 7.8 K in December 2000 at 1 hPa, which is
207 much larger than the maximum of 4.3 K in June 2002 at 3 hPa in the SH. At 35° N/S,
208 significant AO of the Q16W1 amplitude is concentrated only in the height of 10–1 hPa, with
209 peak amplitude also appearing in winter months. At 10°N/S, the amplitudes are smaller than
210 those at middle and high latitudes, with maximum peak smaller than 1.2 K, and the annual
211 variation of wave amplitudes still exists but is not as clear as those in the middle and high
212 latitudes. Besides the annual variation, the wave amplitude also displays SAO above 5 hPa
213 and QBO above 20 hPa.

214 **4. Response to the quasi-biannual oscillation**

215 The latitude-pressure patterns of the monthly mean Q16W1 amplitude response to the
216 QBO1 and QBO2 components, those regression coefficients E and F are calculated by Eq.(2),
217 are shown in Figure 5. As expected, significant positive response to QBO1 at low latitudes
218 (30°N–30°S) from 100 hPa to 50 hPa can be observed, and this response is almost
219 symmetrical about the equator. Besides the low latitude response, strong response can also be
220 clearly seen in the higher stratosphere at the middle and high latitudes. In the NH, the strong

positive and negative response to QBO1 occur at 40°N–75°N, 10–1 hPa and 50°N–85°N, 100–30 hPa, with a positive maximum of 0.12 K at 60°N, 3 hPa and a negative maximum magnitude of ~0.06 K at 72.5°N, 50 hPa, respectively. Lu et al. (2020) explained the high latitude response to the context of Holton-Tan effect, that is more planetary-scale Rossby waves of zonal wave-number 1 can propagate upward to higher stratosphere via high-latitude waveguide during QBO's easterly phase in winters and successive Rossby wave breaking events occur in the middle stratosphere in the middle-high latitudes during QBO's westerly phase in winters. In the SH, the response to the QBO1 illustrates a different pattern. The positive value region is mainly concentrated in mid-latitudes, that is in 25°–55°S, 20–1 hPa, with a positive peak of ~0.11 K at 35°S, 7 hPa.

The response to the QBO2 shown in Figure 5(b) illustrates a different pattern. The response to the QBO2 is mainly negative, which is attributed to the phase difference between the QBO1 and QBO2 wind fields. At low latitudes, the response has weak negative largest values of –0.04 K/m/s at 30°N–30°S from 50 hPa to 30 hPa and are nearly symmetrical around the equator. Similar to the response to the QBO1, the response to the QBO2 has the strongest value at higher latitudes and heights but with a negative peak of –0.16 K/m/s at 62.5°N at 2 hPa. Moreover, the stronger negative response at high latitudes appears only in the NH, exhibiting significant hemispheric asymmetry, which is obviously different from the response to the QBO1.

Our multiple regression analysis results don't show statistically significant responses of Q16W1 amplitude to the ENSO and solar cycle.

5. Long-term trend

243 Figure 6 displays the long-term trend in the monthly mean Q16W1 amplitude in 39
244 years as a function of pressure and latitude. The spatial regions of the significant positive trend
245 regions are almost consistent with those of the strong Q16W1 climatological amplitude as
246 highlighted in Figure 3, which indicates that the wave activities in the mid-upper stratosphere
247 are generally strengthening. It is obvious that the prominent positive trend appears in 20–1 hPa
248 in the NH and 7–1 hPa in the SH, respectively, and it is asymmetric about the equator, with a
249 larger positive trend in the NH. The positive trend increases with height from 30 hPa to 3 hPa
250 and then decreases with height in the NH. Moreover, with increasing latitude in both
251 hemispheres, the positive trend increases poleward, reaches a maximum in the mid-high
252 latitudes and then decreases with latitude. In the NH, the trend has a peak of 0.21 K/decade at
253 3 hPa around the latitude of 67.5°N. In the SH, the positive peak of 0.10 K/decade occurs at
254 3–2 hPa around the latitude of 60°S. A negative trend occurs below 300 hPa, especially at high
255 latitudes in the NH, with a peak negative trend of –0.08 K/decade at 950 hPa around the
256 latitude of 75°N.

257 Some previous studies have revealed the significant seasonal variation in Q16W1
258 (Williams and Avery 1992; Luo et al. 2002b; Hibbins et al. 2009; Day and Mitchell 2010).
259 Here, the Q16W1 amplitude trend in four seasons are investigated. We take December,
260 January, and February to represent the NH winter and SH summer, and March to May, June to
261 August, and September to November to represent the NH (SH) spring (autumn), summer
262 (winter), and autumn (spring), respectively. In each season in each year, there are three values
263 in the monthly mean Q16W1 amplitude. Thus, in the calculation of the trend in each season, a
264 time series of wave amplitudes of 117 months in 39 years are obtained. Similar processes

were performed on the indices of $F_{10.7cm}$, the multivariate ENSO index (MEI) and the time series of QBO, et, al. These time series were substituted into Equation (2) to calculate the trend in each season. Then, in each season, all month dependent trends were averaged to specify the trend in this season. From Figure 7, it can be seen that the positive trends are in 40°N–85°N, 20–1 hPa and 70°S–80°S, 3–2 hPa in spring, 50°N–82.5°N, 3–1 hPa and 20°S–62.5°S, 5–1 hPa in autumn, and 30°N–87.5°N, 30–1 hPa and 20°S–85°S, 7–1 hPa in winter. The negative trends are located near the ground at high latitudes of spring and winter in the NH. The strong enhancement trend is generally consistent with the latitude, height, and seasonal changes of the climatological mean peak amplitude, and generally appears in the mid-high latitudes and high stratosphere in winter. The strongest trend appears in the NH winter (shown in Figure 7d), with a peak of 0.54 K/decade at 3 hPa around the latitude of 67.5°N, which is significantly larger than trend in the SH winter (shown in Figure 7b), in which the positive peak of 0.19 K/decade occurs at 3 hPa around the latitude of 50°S, indicating the obvious hemispheric asymmetry in Q16W1 amplitude trend.

From above analyses, it can be significantly seen that the Q16W1 climatological amplitudes and trends appear in middle and high latitudes. Dickinson (1968) proposed a polar waveguide theory, which predicted that PWs will propagate from the troposphere to the stratosphere at high latitudes. Mastuno (1970) obtained similar results using the quasi-geostrophic model. Luo et al. (2002a; 2002b) confirmed that the westward-traveling 16-day wave with a small phase velocity can propagate upward through the winter polar night jet to reach the MLT region only in an eastward background flow of moderate speed which is present in the winter hemisphere. The zonal wind was confirmed by Smith (1983) to be a key

287 factor for the vertical propagation and dissipation of PWs. For simplification, a PW can
288 propagate through a region only when the PW zonal phase velocity c and background zonal
289 wind u_o satisfy the following conditions (McDonald et al. 2011):

$$290 \quad 0 < u_o - c < \frac{\beta}{(k^2 + l^2) + \frac{f_o^2}{4H^2N^2}} \equiv U_c \quad (3)$$

291 where $k = 2\pi/\lambda_x$, $l = 2\pi/\lambda_y$ is the zonal and meridional wavenumber of the Q16W1, in
292 which λ_x and λ_y are the zonal and meridional wavelengths of the Q16W1, respectively. f_o
293 and β represent the Coriolis parameter and Rossby parameter, respectively. The zonal phase
294 velocity of the Q16W1 $c = \omega/k$, where $\omega = 2\pi/T$ is the frequency of the Q16W1. The
295 positive (negative) values of u_o and c indicate the eastward (westward) direction. U_c is
296 the critical Rossby velocity determined by the PW. Equation (3) shows that weak eastward
297 zonal wind is favourable for Q16W1 propagation, otherwise, energy is trapped/reflected in
298 regions where the zonal winds are westward or strongly eastward. Therefore, the zonal mean
299 wind plays an important role in the PW propagation and its long-term variation may be related
300 to the long-term trend of Q16W1 amplitude.

301 Figure 8 displays the trends and the climatological distributions of monthly mean
302 zonal wind in four seasons. Combined with Figure 7, it is shown that the amplitude of the
303 Q16W1 is usually strong in regions where the background zonal wind is weak eastward wind
304 (Day et al. 2011). The zonal wind trend has significant positive values in the height range
305 from 1000 hPa to 7 hPa in mid-high latitudes of the SH summer. More interestingly, the zonal
306 wind trend has significant negative values in the height range from 1000 hPa to 50 hPa at high
307 latitudes in the NH winter, with a negative peak of -1.4m/s/decade at 50 hPa around the
308 latitude of 67.5°N. Another negative trend of the zonal wind appears in 30°S–50°S, at 30–20

309 hPa. It should be noted that these negative trend regions correspond to the climatological
 310 eastward wind region, implying the gradual weakening of the eastward wind u_o . This
 311 wakened eastward wind will lead to a more favourable background for the
 312 upward-propagation of the Q16W1, which in turn, may cause an increasing trend of wave
 313 amplitude. Obviously, the negative zonal wind trend could contribute to the positive trend of
 314 the Q16W1 amplitude.

315 It is known that the mean flow barotropic and baroclinic instabilities are important in
 316 local excitation for PWs (Hartmann 1983; Huang et al. 2021; William and Leslie 1991). Then,
 317 we will investigate possible influences of the local excitation mechanism on the trend of the
 318 Q16W1 amplitude by analysing the mean flow instability. A necessary condition for
 319 instability of the mean flow is that the quasi-geostrophic potential vorticity gradient (\bar{q}_ϕ)
 320 must change sign somewhere in the flow domain (Andrews et al. 1987). Then, the overturning
 321 of the \bar{q}_ϕ can be regarded as the local instability, which means that relatively small \bar{q}_ϕ
 322 implies high probability of the overturning of \bar{q}_ϕ , as well as the local instability (Lu et al.
 323 2020). \bar{q}_ϕ can be expressed as:

$$324 \quad \bar{q}_\phi = 2\Omega \cos \phi - \left[\frac{(\bar{u} \cos \phi)_\phi}{a \cos \phi} \right]_\phi - \frac{a}{\rho_o} \left(\frac{\rho_o f^2}{N^2} \bar{u}_z \right)_z \quad (4)$$

325 Where overbar, prime and subscript denote respectively zonal average and derivative; u , ρ_o ,
 326 a , Ω , ϕ , and f represent the zonal wind, background density, Earth radius, angular velocity
 327 of the Earth, latitude and Coriolis parameter, respectively; z is the altitude above the Earth's
 328 surface; N is the buoyancy frequency, which is specified by calculating from
 329 $N^2 = \frac{g}{T} \left(\frac{\partial \bar{T}}{\partial z} + \frac{g}{c_p} \right)$, where g , \bar{T} , and c_p are the height-dependent gravitational acceleration,

330 background temperature, and specific heat at constant pressure, respectively.

331 Considering validity limitations of the quasi-geostrophic approximation near the
332 equator and surface, and numerical singularities near the poles, the climatological
333 distributions and the negative trends of monthly mean \bar{q}_ϕ values in two latitudes zones,
334 those are 15°S – 85°S and 15°N – 85°N , and altitude above 500 hPa are shown in Figure 9. In the
335 NH, it is intriguing to note that in all seasons, the monthly mean \bar{q}_ϕ values are mostly
336 positive in almost all regions except at about 300 hPa of the low and middle latitudes and in
337 the high latitudes of summer. Large values of \bar{q}_ϕ are found in the troposphere. We
338 concentrate on the regions with relatively small \bar{q}_ϕ and negative \bar{q}_ϕ trend, where
339 increasing instability trend is most likely to occur. These regions are located in 70°N – 80°N
340 from 5 hPa to 2 hPa in summer, 75°N – 85°N from 200 hPa to 100 hPa in autumn and 55°N –
341 75°N from 250 hPa to 70 hPa. Combined with the wave trend in the NH in Figure 7 and the
342 probability of wave upward propagation, the increased possibility of instability could partly
343 explain the Q16W1 amplitude trends in autumn and winter.

344 Similar to that in the NH, the climatological \bar{q}_ϕ in the SH in Figure 9 is also mainly
345 positive, interestingly, it has significant large positive value in the middle and high latitudes of
346 the stratosphere in both spring and winter and negative value at high latitudes in all seasons
347 except autumn. The regions located in 57.5°S – 62.5°S at 2 hPa in spring, high latitudes from
348 200 hPa to 100 hPa in autumn and 30°S – 40°S at 50–20 hPa in winter, where the \bar{q}_ϕ
349 represent negative trends, indicating an enhancement of instability. Generally, the increasing
350 trend of instability located in 50°N – 82.5°N from 3 hPa to 1 hPa in autumn and 30°N – 87.5°N
351 from 30 hPa to 1 hPa in winter in the NH and in 70°S – 80°S , from 3 hPa to 2 hPa in spring,

352 20°S–62.5°S from 5 hPa to 1 hPa in autumn and 20°S–85°S from 7 hPa to 1 hPa in winter in
353 the SH, may contribute to the increasing trend of Q16W1 amplitude.

354 **6. Summary**

355 The Q16W1 was shown to be the dominant mode of 16DW globally from the surface
356 to the stratopause by analysing the ERA–Interim reanalysis datasets from February 1979 to
357 January 2018. The response of the monthly mean Q16W1 amplitude to QBO, ENSO and solar
358 activity and their linear trend were investigated by multiple regression analysis. Possible
359 mechanisms of inducing the trend of the Q16W1 in NH winter are discussed. The primary
360 results are summarized as follows.

361 For the 39 years climatological mean value, strong Q16W1 occurs in the upper
362 stratosphere at high latitudes in both hemispheres, and the wave amplitude is stronger in the
363 NH than in the SH. The Q16W1 present obvious seasonal variation, that is, strong in winter
364 and weak in summer. This seasonal variation is more prominent in the middle and high
365 latitudes. The Q16W1 in the stratosphere exhibits AO, especially in high latitudes, where the
366 AO is evident in the whole stratosphere.

367 The QBO1 signatures of the Q16W1 amplitude are mainly positive and more
368 pronounced in the stratosphere. In low latitudes (30°N–30°S) at 100–50 hPa, the positive
369 signatures are almost symmetrical around the equator. The strongest positive signatures occur
370 at higher latitudes and heights, i.e., in 35°N–80°N and 20°S–55°S at 10–1 hPa. Because of the
371 phase difference between the QBO1 and QBO2 wind components, the QBO2 signatures of
372 the Q16W1 amplitude are mainly negative. Notably, unlike the QBO1 signatures, the QBO2
373 signature of the Q16W1 amplitude exhibits significant hemispheric asymmetry, with strong

374 negative signatures at high latitudes appearing only in the NH. No obvious responses to solar
375 activity and ENSO are found.

376 The long-term trend of the monthly mean Q16W1 amplitude is generally positive and
377 mainly concentrated in the stratosphere. The trend is asymmetric around the equator at 30–1
378 hPa and significantly stronger in the NH than in the SH. Weak negative trend is mainly
379 located below 300 hPa at high latitudes in the NH.

380 The trend of the monthly mean Q16W1 amplitude has evident seasonal variation. The
381 positive trend is largest in winter at 30–1 hPa at all latitudes in both hemispheres. To
382 investigate the possible causes of the trend of Q16W1, we calculated the long-term trend of
383 the monthly mean zonal wind and \bar{q}_ϕ in each of the four seasons. In winter of both
384 hemispheres, the weakening trend of eastward zonal wind contributes to the increasing trend
385 of the Q16W1 amplitude because the weak eastward zonal wind is favourable for Q16W1
386 propagation. Moreover, in autumn and winter in the NH and in spring, autumn and winter in
387 the SH, increasing trend of instability will enhance the wave excitation and thus lead to the
388 increasing trend of the Q16W1 amplitude.

389

390 **Declarations**

391 **Availability of data and materials**

392 The ERA-Interim data set were freely downloaded from the European Centre for Medium-Range
393 Weather Forecasts (<https://apps.ecmwf.int/datasets/data/interim-full-daily/levtype=pl/>), The $F_{10.7\text{cm}}$
394 solar flux data and multivariate ENSO index data were downloaded from
395 <http://www.esrl.noaa.gov/psd/>, and the QBO data series were from

396 <http://www.geo.fu-berlin.de/en/met/ag/strat/produkte/qbo/index.html>.

397

398 **Competing interests**

399 The authors declare that they have no competing interests.

400

401 **Funding**

402 The present work is jointly supported by the National Natural Science Foundation of China under

403 Grant Numbers 41874177 and 41874178.

404

405 **Authors' contributions**

406 Wen Tao TANG carried out the reanalysis data processing and wrote the first draft of the paper. Shao

407 Dong ZHANG conceived and coordinated this study and also assisted in manuscript preparation.

408 Chun Ming HUANG performed analyses related to the present study, and interpreted the results. Kai

409 Ming HUANG, Yun GONG, and Quan GAN contributed to the scientific interpretation. All

410 authors read and approved the final manuscript.

411

412 **Acknowledgements**

413 We thank the European Centre for Medium-Range Weather Forecasts (ECMWF) for the dissemination

414 of ERA-Interim data.

415

416 **References**

417 Alexander SP, Shepherd MG (2010) Planetary wave activity in the polar lower stratosphere. Atmos

- 418 Chem Phys 10(2):707–718. <https://doi.org/10.5194/acp-10-707-2010>
- 419 Amitava G, Paulo PB, Barclay RC, Ricardo AB, Nelson JS (2016) Latitudinal variability of the
420 quasi-16-day wave in the middle atmosphere over Brazilian stations. Ann Geophys 34:411–419.
421 <https://doi.org/10.5194/angeo-34-411-2016>
- 422 Andrews DG, Holton JR, Leovy CB (1987) Middle atmosphere dynamics. New York NY USA:
423 Academic Press.
- 424 Charney JG, Drazin PG (1961) Propagation of planetary-scale disturbances from lower into upper
425 atmosphere. J Geophys Res 66:83–109. <https://doi.org/10.1029/JZ066i001p00083>
- 426 Das SS, Kumar KK, Veena SB, Ramkumar G (2010) Simultaneous observation of quasi 16 day wave
427 in the mesospheric winds and temperature over low latitudes with the SKiYMET radar. Radio Sci
428 45:RS6014. <https://doi.org/10.1029/2009RS004300>
- 429 Day KA, Hibbins RE, Mitchell NJ (2011) Aura MLS observations of the westward-propagating s=1,
430 16-day planetary wave in the stratosphere, mesosphere and lower thermosphere. Atmos Chem
431 Phys 11:4149–4161. <https://doi.org/10.5194/acp-11-4149-2011>
- 432 Day KA, Mitchell NJ (2010) The 16-day wave in the Arctic and Antarctic mesosphere and lower
433 thermosphere. Atmos Chem Phys 10:1461–1472. <https://doi.org/10.5194/acp-10-1461-2010>
- 434 Dickinson RE (1968) Planetary Rossby waves propagating vertically through weak westerly wind
435 wave guides. J Atmos Sci 25:984–1002
- 436 Espy PJ, Stegman J, Witt G (1997) Interannual variations of the quasi-16-day oscillation in the polar
437 summer mesospheric temperature. J Geophys Res 102:1983–1990.
438 <https://doi.org/10.1029/96JD02717>
- 439 Gan Q, Du J, Fomichev VI, Ward WE, Beagley SR, Zhang S, Yue J (2017) Temperature responses to

440 the 11 year solar cycle in the mesosphere from the 31 year (1979-2010) extended Canadian
441 Middle Atmosphere Model simulations and a comparison with the 14 year (2002-2015)
442 TIMED/SABER observations. J Geophys Res Space Phys 122:4801–4818,
443 <https://doi.org/10.1002/2016JA023564>

444 Gan Q, Oberheide J, Pedatella NM (2018) Sources, sinks, and propagation characteristics of the quasi
445 6-day wave and its impact on the residual mean circulation. J Geophys Res Atmos 123:9152–
446 9170. <https://doi.org/10.1029/2018JD028553>

447 Gong Y, Wang H, Ma Z, Zhang S, Zhou Q, Huang C, Huang K (2019) A statistical analysis of the
448 propagating quasi 16-day waves at high latitudes and their response to sudden stratospheric
449 warmings from 2005 to 2018. J Geophys Res Atmos 124:12617–12630.
450 <https://doi.org/10.1029/2019JD031482>

451 Hartmann DL (1983) Barotropic instability of the polar night jet stream. J Atmos Sci 40:817–835.
452 [https://doi.org/10.1175/1520-0469\(1983\)040<0817:BIOTPN>2.0.CO;2](https://doi.org/10.1175/1520-0469(1983)040<0817:BIOTPN>2.0.CO;2)

453 Huang C, Li W, Zhang S, Chen G, Huang K, Gong Y (2021) Investigation of dominant traveling 10-
454 day wave components using long-term MERRA-2 database. Earth Planets Space, 73:85.
455 <https://doi.org/10.1186/s40623-021-01410-7>

456 Huang C, Zhang S, Chen G, Zhang S, Huang K (2017) Planetary wave characteristics in the lower
457 atmosphere over Xianghe (117.00°E, 39.77°N), China, revealed by the Beijing MST radar and
458 MERRA data. J Geophys Res Atmos 122:9745–9758. <https://doi.org/10.1002/2017JD027029>

459 Huang KM, Liu AZ, Zhang SD, Yi F, Huang CM, Gan Q, Gong Y, Zhang YH (2013) A nonlinear
460 interaction event between 16-day wave and a diurnal tide from meteor radar observations. Ann
461 Geophys 31:2039–2048. <https://doi.org/10.5194/angeo-31-2039-2013>

- 462 Hu Y, Tung KK (2002) Interannual and decadal variations of planetary wave activity, stratospheric
463 cooling, and northern hemisphere annular mode. *J Climate* 15:1659–1673.
464 [https://doi.org/10.1175/1520-0442\(2002\)015<1659:IADVOP>2.0.CO;2](https://doi.org/10.1175/1520-0442(2002)015<1659:IADVOP>2.0.CO;2)
- 465 Hu D, Guo Y, Guan Z (2019) Recent Weakening in the Stratospheric Planetary Wave Intensity in Early
466 Winter. *Geophys Res Lett* 46:3953–3962. <https://doi.org/10.1029/2019GL082113>
- 467 Hibbins RE, Jarvis JM, Ford EAK (2009) Quasi-biennial oscillation influence on long-period PWs in
468 the Antarctic upper mesosphere. *J Geophys Res* 114:DO9109.
469 <https://doi.org/10.1029/2008JD011174>
- 470 Hitchman MH, Huesmann AS (2007) A seasonal climatology of Rossby wave breaking in the 330–
471 2000 K layer. *J Atmos Sci* 64:1922–1940.
- 472 Kallberg P, Simmons A, Uppala S, Fuentes M (2004) The ERA-40 archive. ERA-40 Project Rep.
473 Series 17, European Centre for Medium-Range Weather Forecasts, Reading, United Kingdom, 31
474 pp.
- 475 Kozubek M, Krizan P, Lastovicka J (2017) Comparison of the long-term trends in stratospheric
476 dynamics of four reanalyses. *Ann Geophys* 35:279–294.
477 <https://doi.org/10.5194/angeo-35-279-2017>
- 478 Kutner MH, Nachtsheim CJ, Neter J, Li W (2004) Applied Linear Statistical Models, 5th ed, pp:40–88
479 and pp:214–247. McGraw-Hill/Irwin, San Francisco, Calif
- 480 Lu H, Hitchman MH, Gray LJ, Anstey JA, Osprey SM (2020) On the role of Rossby wave breaking in
481 the quasi-biennial modulation of the stratospheric polar vortex during boreal winter. *Q J R
482 Meteorol Soc* 146:1939–1959. <https://doi.org/10.1002/qj.3775>
- 483 Luo Y, Manson AH, Meek CE, Meyer CK, Burrage MD, Fritts DC, Hall CM, Hocking WK,

- 484 MacDougall J, Riggan DM, Vincent RA (2002b) The 16-day planetary waves: multi-MF radar
485 observations from the arctic to equator and comparisons with the HRDI measurements and the
486 GSWM modelling results. *Ann Geophys* 20:691–709. <https://doi.org/10.5194/angeo-20-691-2002>
- 487 Luo Y, Manson AH, Meek CE, Thayaparan T, MacDougall J, Hocking WK (2002a) The 16-day wave
488 in the mesosphere and the lower thermosphere: simultaneous observations at Saskatoon (52°N,
489 107°W), London (43°N, 81°W), Canada. *J Atmos Terr Phys* 64:1287–1307.
490 [https://doi.org/10.1016/S1364-6826\(02\)00042-1](https://doi.org/10.1016/S1364-6826(02)00042-1)
- 491 Matsuno T (1970) Vertical propagation of stationary planetary waves in winter Northern Hemisphere.
492 *J Atmos Sci* 27(6): 871–883.
493 [https://doi.org/10.1175/1520-0469\(1970\)027<0871:Vpospw>2.0.Co;2](https://doi.org/10.1175/1520-0469(1970)027<0871:Vpospw>2.0.Co;2)
- 494 Mitchell NJ, Middleton HR, Beard AG, Williams PJS, Muller HG (1999) The 16-day planetary wave
495 in the mesosphere and lower thermosphere. *Ann Geophys* 17:1447–1456.
496 <https://doi.org/10.1007/s00585-999-1447-9>
- 497 McDonald AJ, Hibbins RE, Jarvis JM (2011) Properties of the quasi-16 day wave derived from EOS
498 MLS observations. *J Geophys Res Atmos* 116:D06112. <https://doi.org/10.1029/2010JD014719>
- 499 Meek CE, Manson AH (2009) Summer planetary-scale oscillations: aura MLS temperature compared
500 with ground-based radar wind. *Ann Geophys* 27:1763–1774.
501 <https://doi.org/10.5194/angeo-27-1763-2009>
- 502 Randel WJ, Wu F, Stolarski R (2002) Changes in column ozone correlated with the stratospheric E-P
503 flux. *J Meteor Soc Japan* 80:849–862. <https://doi.org/10.2151/jmsj.80.849>
- 504 Salby ML (1981a) Rossby Normal Modes in Nonuniform Background Configurations. Part I: Simple
505 fields. *J Atmos Sci* 38:1803–1826.

- 506 https://doi.org/10.1175/1520-0469(1981)038<1803:RNMINB>2.0.CO;2
- 507 Salby ML (1981b) Rossby Normal Modes in Nonuniform Background Configurations. Part II:
508 Equinox and Solstice Conditions. *J Atmos Sci* 38:1827–1840.
- 509 https://doi.org/10.1175/1520-0469(1981)038<1827:RNMINB>2.0.CO;2
- 510 She CY, Krueger DA, Yuan T (2015) Long-term midlatitude mesopause region temperature trend
511 deduced from quarter century (1990–2014) Na lidar observations. *Ann Geophys* 33:363–369.
- 512 https://doi.org/10.5194/angeo-33-363-2015
- 513 Smith AK (1997) Stationary Planetary Waves in upper mesospheric winds. *J Atmos Sci* 54:2129–2145.
514 https://doi.org/10.1175/1520-0469(1997)054<2129:SPWIUM>2.0.CO;2
- 515 Tsuda T, Murayama Y, Wiryosumarto H, Harijono SWB, Kato S (1994) Radiosonde observations of
516 equatorial atmosphere dynamics over Indonesia, 1, Equatorial waves and diurnal tides. *J Geophys
517 Res Atmos* 99:10491–10505. https://doi.org/10.1029/94JD00355
- 518 Vineeth C, Pant TK, Kumar KK, Sumod SG (2010) Tropical connection to the polar stratospheric
519 sudden warming through quasi 16-day planetary wave. *Ann Geophys* 28:2007–2013.
520 https://doi.org/10.5194/angeo-28-2007-2010
- 521 Weber M, Coldewey-Egbers M, Fioletov VE, Frith SM, Wild JD, Burrows JP, Long CS, Loyola D
522 (2018) Total ozone trends from 1979 to 2016 derived from five merged observational datasets—the
523 emergence into ozone recovery. *Atmos Chem Phys* 18:2097–2117.
524 https://doi.org/10.5194/acp-18-2097-2018
- 525 Wallace JM, Panetta RL, Estberg J (1993) Representation of the equatorial stratospheric quasi-biennial
526 oscillation in EOF phase space. *J Atmos Sci* 50:1751–1762.
527 https://doi.org/10.1175/1520-0469(1993)050<1751:ROTESQ>2.0.CO;2

528 Williams CR, Avery SK (1992) Analysis of long-period waves using the
529 mesosphere-stratosphere-troposphere radar at poker flats, Alaska. *J Geophys Res Atmos*
530 97:20855–20861. <https://doi.org/10.1029/92JD02052>

531 William JR, Leslie RL (1991) Dynamics of the 4-day wave in the Southern-Hemisphere polar
532 stratosphere. *J Atmos Sci* **48**:2496–2508.
533 [https://doi.org/10.1175/1520-0469\(1991\)048<2496:DOTDWI>2.0.CO;2](https://doi.org/10.1175/1520-0469(1991)048<2496:DOTDWI>2.0.CO;2)

534 Wu DL, Hays PB, Skinner WR (1995) A least squares method for spectral analysis of space-time
535 series, *J Atmos Sci* **52**:3501–3511.
536 [https://doi.org/10.1175/1520-0469\(1995\)052<3501:ALSMFS>2.0.CO;2](https://doi.org/10.1175/1520-0469(1995)052<3501:ALSMFS>2.0.CO;2)

537

538

539

540

541

542

543

544

545

546

547

548

549

550

551 **Figure captions:**

552 **Fig. 1** Mean frequency-wavenumber spectrum of temperature (in K) from February 1979 to January
553 2018 (39 years in total) at 37 pressure levels from 1000 hPa to 1 hPa. W (E) represents westward
554 (eastward) propagation.

555 **Fig. 2** The time series of (a) SC index (F10.7cm flux), (b) multivariate ENSO index (MEI), and (c) the
556 QBO indices on the monthly basis from February 1979 to January 2018, respectively.

557 **Fig. 3** The latitude-pressure distribution of the monthly mean Q16W1 amplitude averaged over 39
558 years from the ERA-interim temperature data set.

559 **Fig. 4** Month-latitude sections of the monthly and zonal-mean Q16W1 amplitude at high, middle, and
560 low latitudes in the NH (three upper rows) and SH (three lower rows), respectively.

561 **Fig. 5** Latitude-pressure sections of the responses of the monthly-mean Q16W1 amplitude to (a)
562 QBO1 and (b) QBO2, respectively. Only the results with the confidence level at/above 95% are
563 plotted in contours. The solid and dashed contours denote the positive and negative responses,
564 respectively.

565 **Fig. 6** Long-term trend (in K per decade) as a function of pressure and latitude of the monthly mean
566 Q16W1 amplitude obtained from the 39 years ERA-interim temperature data set. Only the results with
567 the confidence level at/above 95% are plotted in contours. The solid and dashed contours denote the
568 positive and negative trends, respectively.

569 **Fig. 7** Seasonal variation of the Long-term trend (in K per decade) as a function of latitude and
570 pressure of the monthly-mean Q16W1 amplitude from the 39 years ERA-interim temperature data set.
571 The solid and dashed contours denote the positive and negative trends, respectively. The black

572 contours denote the trend with confident level at/above 95%. The colors represents the climatological
573 distributions of the monthly mean Q16W1 amplitude in four seasons.

574 **Fig. 8** Trend (contours, units: m/s/decade) of the monthly mean zonal wind in four seasons derived
575 from the 39 years ERA-interim zonal wind set. The solid and dashed contours denote the positive and
576 negative trends, respectively. The thick black contour represents the 0 value. The stippled regions
577 represent the trends at/above 95% confident level. The colors present the climatological distributions
578 of the monthly mean zonal wind in four seasons.

579 **Fig. 9** Trend (contours, units: $10^{-5} \text{ m}^{-1} \text{ s}^{-1}/\text{decade}$) of the monthly mean \bar{q}_ϕ in four seasons. The
580 dashed contours denote the negative trend. The stippled regions represent the trends at/above 95%
581 confident level. The colors present the climatological distributions of the monthly mean zonal \bar{q}_ϕ in
582 four seasons.

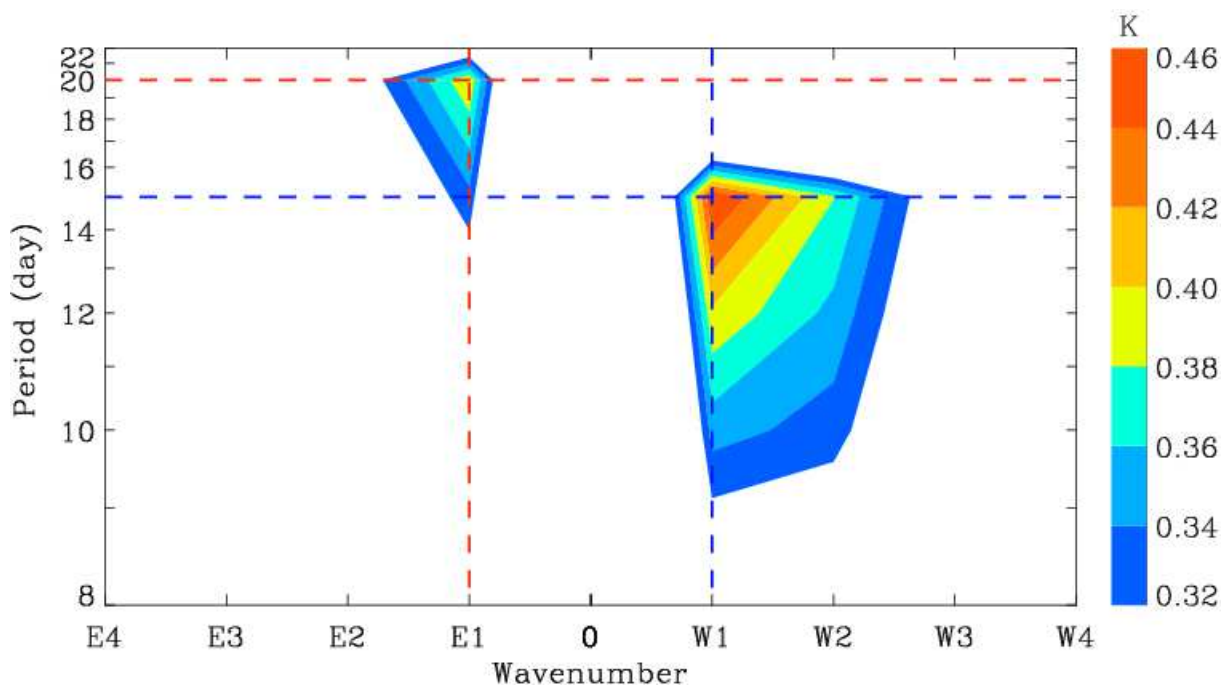
583

584

585

586

587



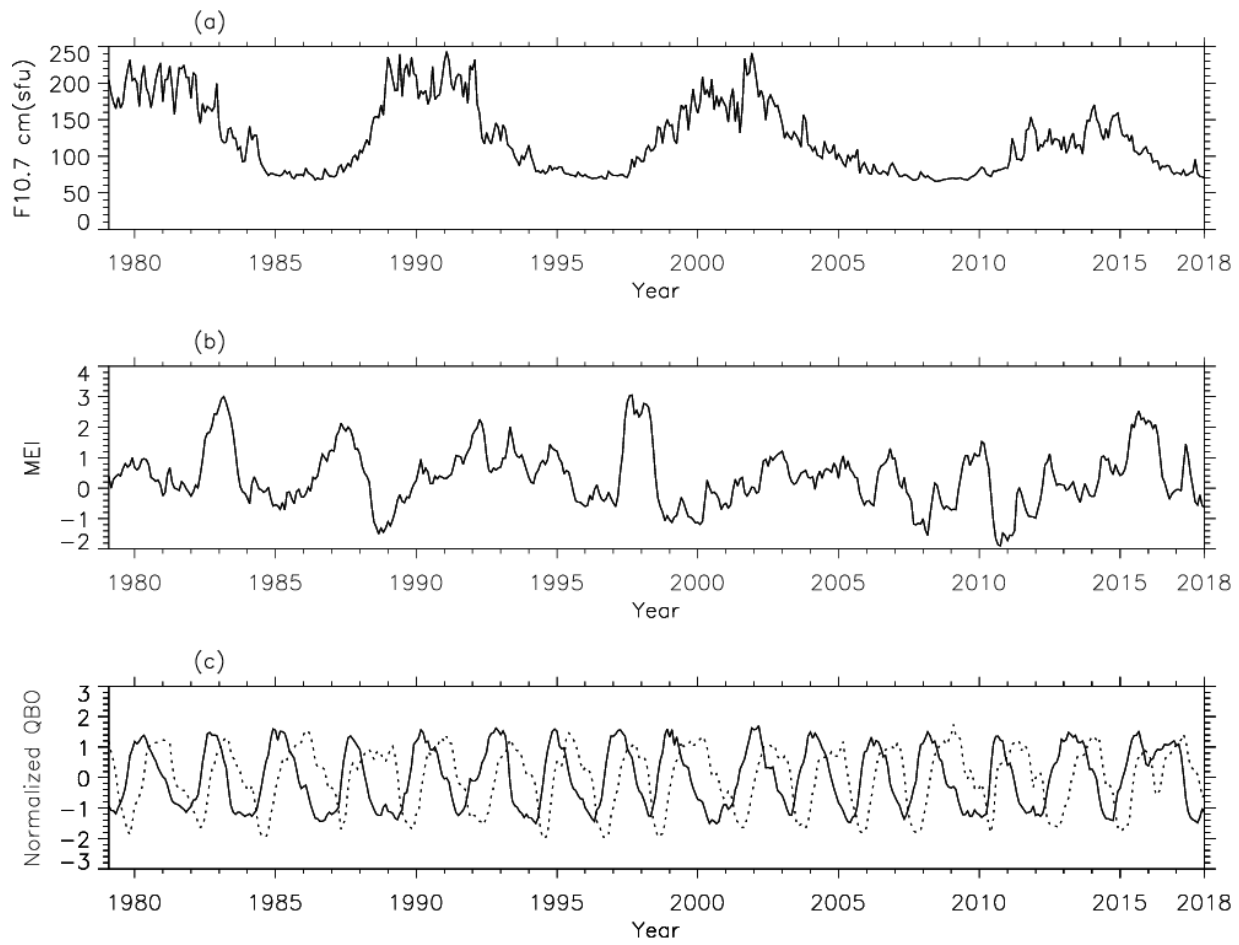
588

589 **Fig. 1** Mean frequency-wavenumber spectrum of temperature (in K) from February 1979 to January

590 2018 (39 years in total) at 37 pressure levels from 1000 hPa to 1 hPa. W (E) represents westward

591 (eastward) propagation.

592



593

594 **Fig. 2** The time series of (a) SC index ($F_{10.7\text{cm}}$ flux), (b) multivariate ENSO index (MEI), and (c) the
 595 QBO indices on the monthly basis from February 1979 to January 2018, respectively.

596

597

598

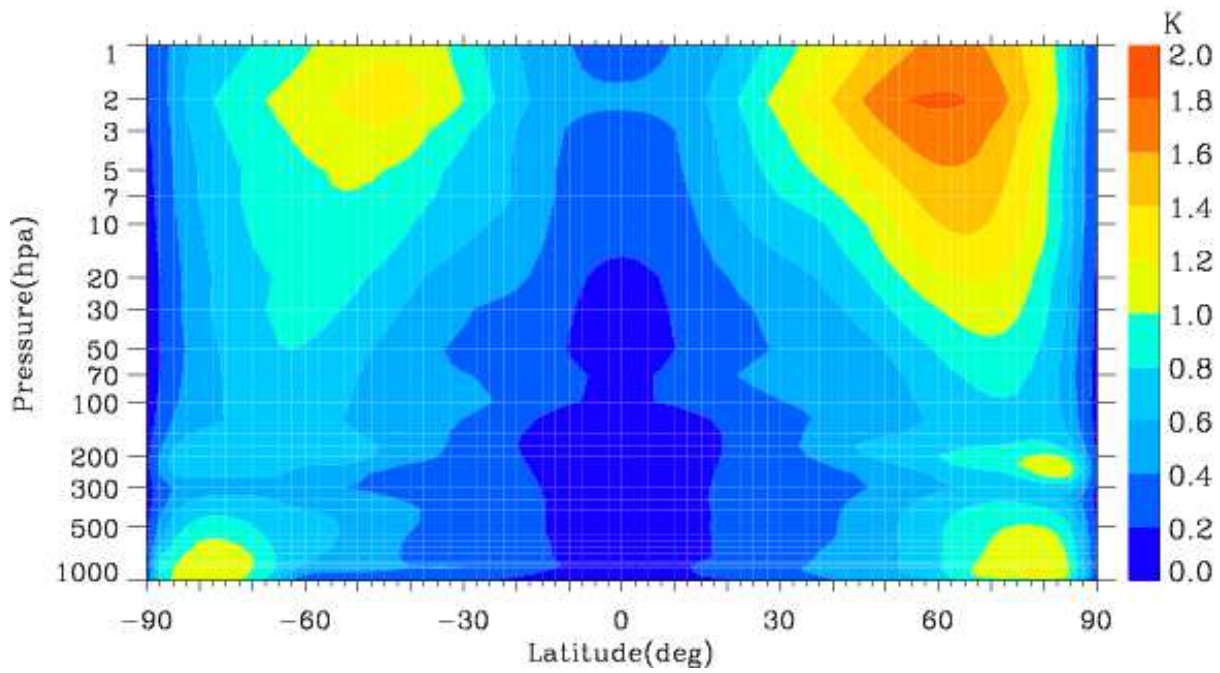
599

600

601

602

603



604

605 **Fig. 3** The latitude-pressure distribution of the monthly mean Q16W1 amplitude averaged over 39
606 years from the ERA-interim temperature data set.

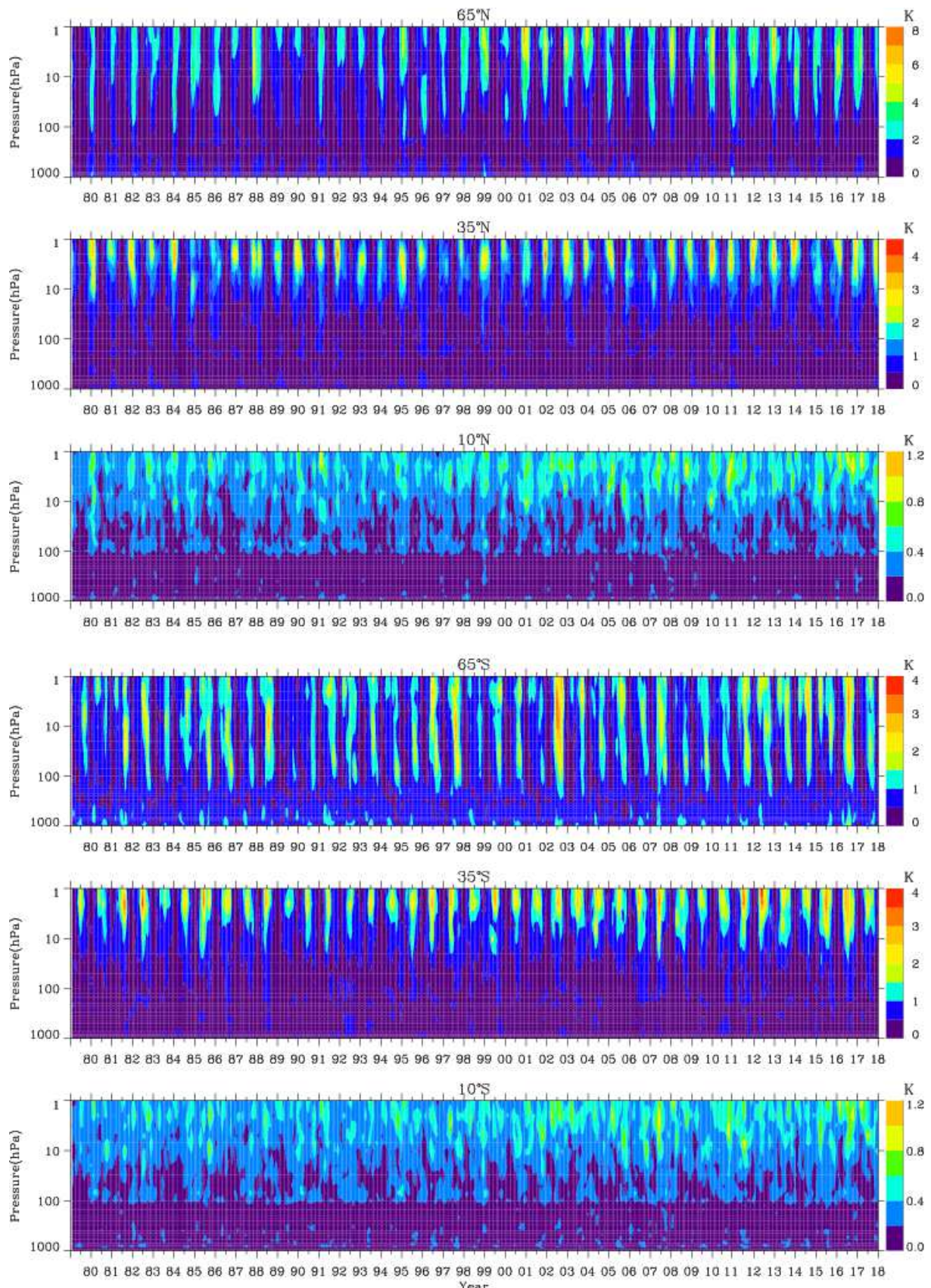
607

608

609

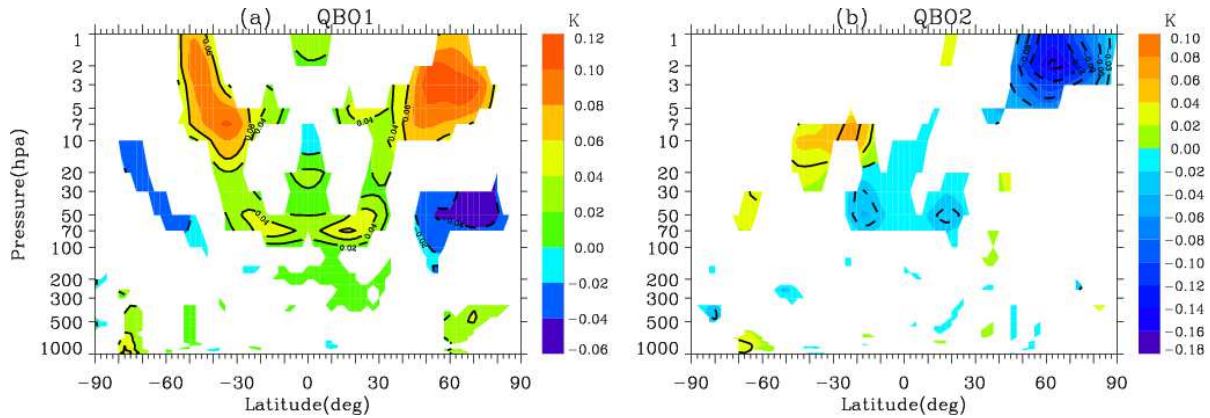
610

611



612

613 **Fig. 4** Month-latitude sections of the monthly and zonal-mean Q16W1 amplitude at high, middle, and
614 low latitudes in the NH (three upper rows) and SH (three lower rows), respectively.



615

616 **Fig. 5** Latitude-pressure sections of the responses of the monthly-mean Q16W1 amplitude to (a)
 617 QBO1 and (b) QBO2, respectively. Only the results with the confidence level at/above 95% are
 618 plotted in contours. The solid and dashed contours denote the positive and negative responses,
 619 respectively.

620

621

622

623

624

625

626

627

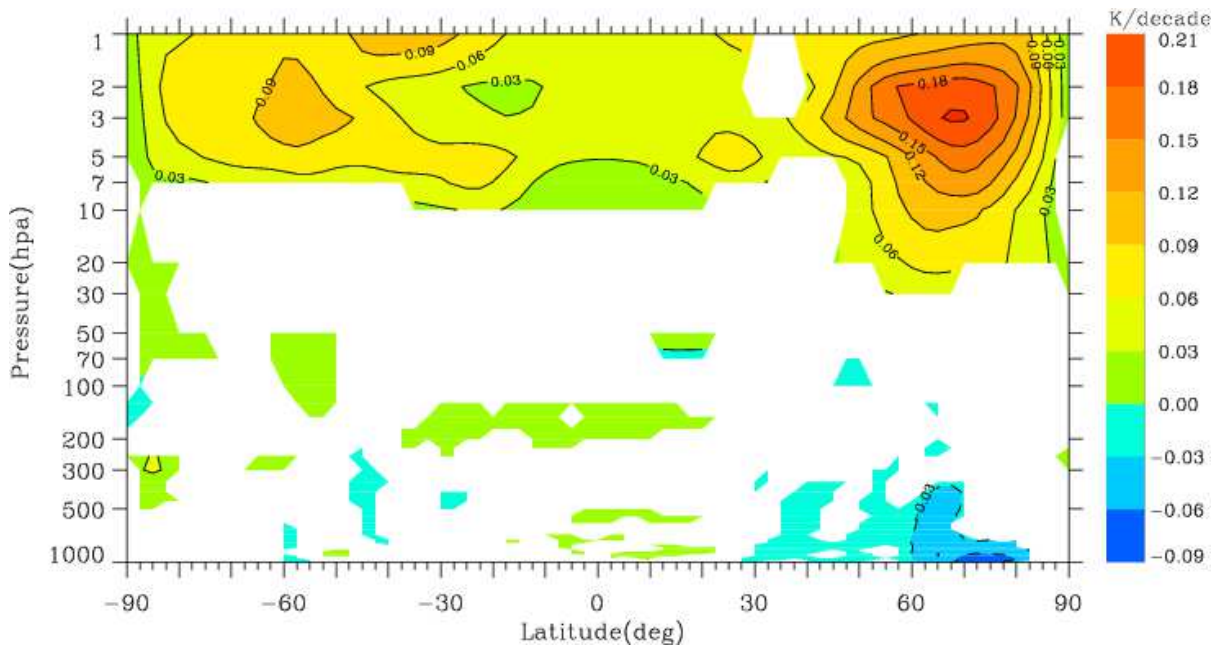
628

629

630

631

632



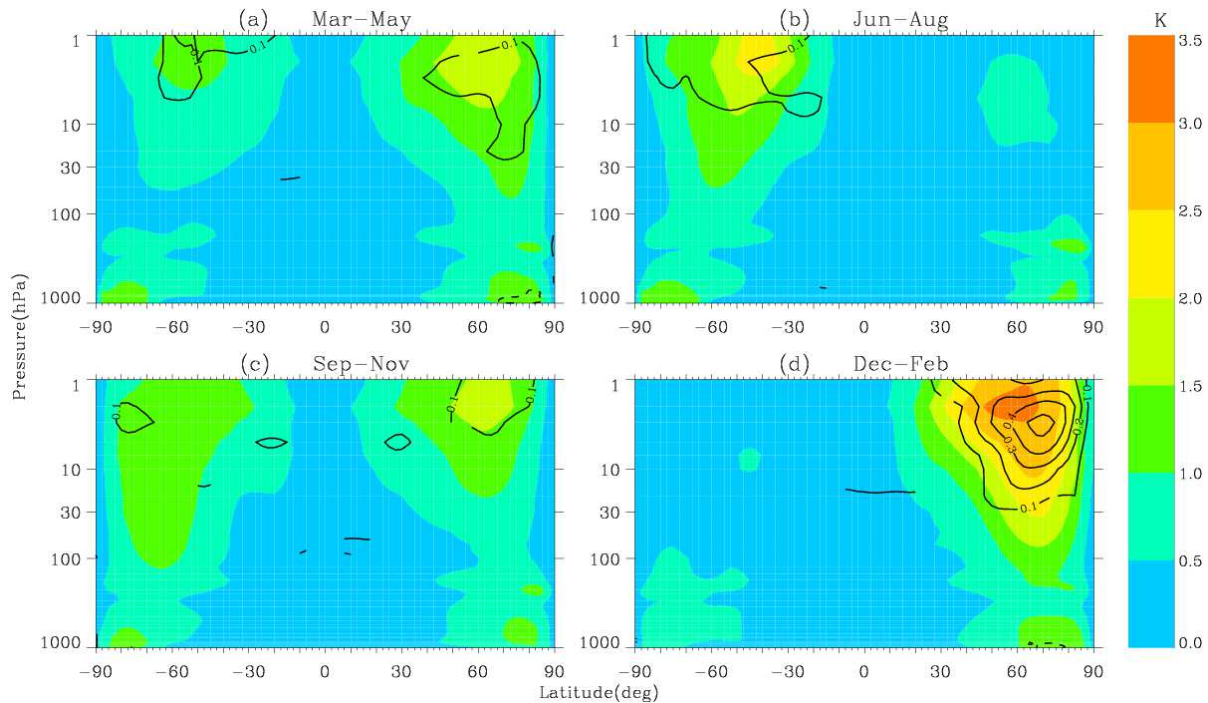
633

634 **Fig. 6** Long-term trend (in K per decade) as a function of pressure and latitude of the monthly mean
 635 Q16W1 amplitude obtained from the 39 years ERA-interim temperature data set. Only the results with
 636 the confidence level at/above 95% are plotted in contours. The solid and dashed contours denote the
 637 positive and negative trends, respectively.

638

639

640



641

642 **Fig. 7** Seasonal variation of the Long-term trend (in K per decade) as a function of latitude and
 643 pressure of the monthly-mean Q16W1 amplitude from the 39 years ERA-interim temperature data set.
 644 The solid and dashed contours denote the positive and negative trends, respectively. The black
 645 contours denote the trend with confident level at/above 95%. The colors represent the climatological
 646 distributions of the monthly mean Q16W1 amplitude in four seasons.

647

648

649

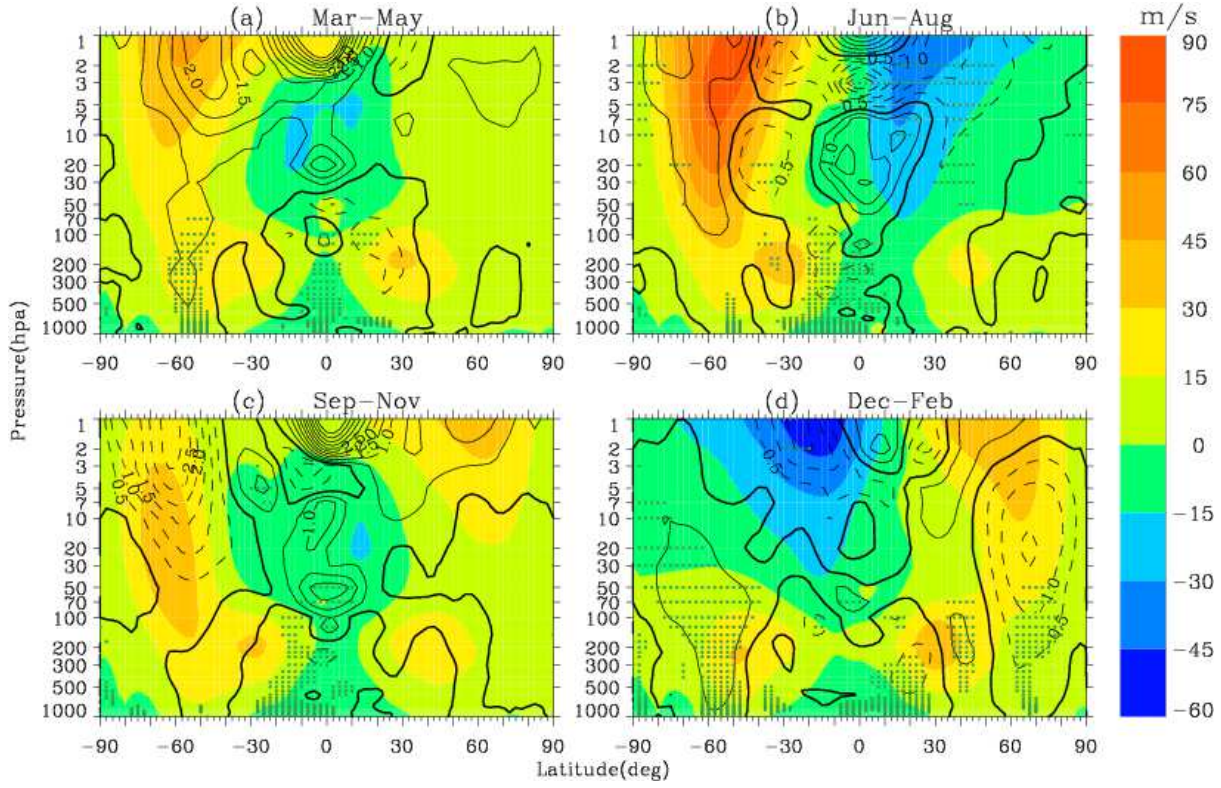
650

651

652

653

654



655

656 **Fig. 8** Trend (contours, units: m/s/decade) of the monthly mean zonal wind in four seasons derived
 657 from the 39 years ERA-interim zonal wind set. The solid and dashed contours denote the positive and
 658 negative trends, respectively. The thick black contour represents the 0 value. The stippled regions
 659 represent the trends at/above 95% confident level. The colors present the climatological distributions
 660 of the monthly mean zonal wind in four seasons.

661

662

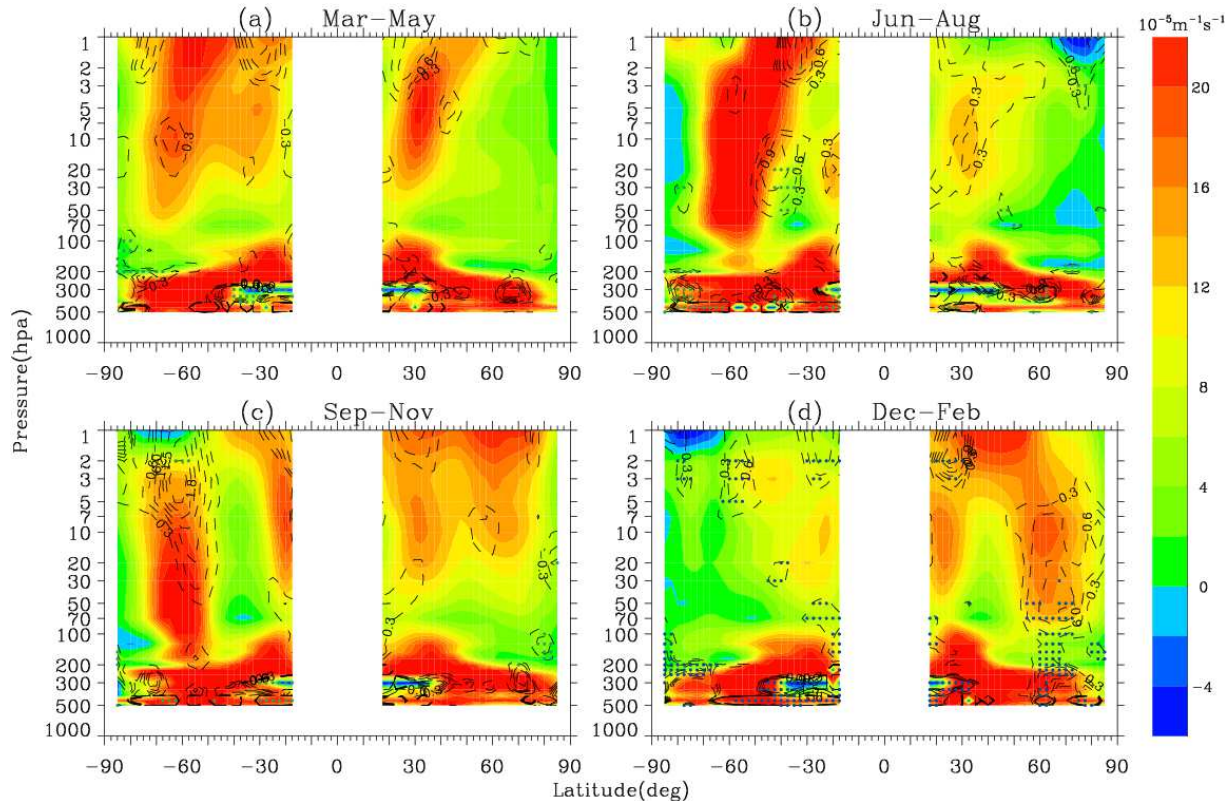
663

664

665

666

667



668

669 **Fig. 9** Trend (contours, units: $10^{-5} \text{ m}^{-1} \text{ s}^{-1}/\text{decade}$) of the monthly mean \bar{q}_ϕ in four seasons. The
 670 dashed contours denote the negative trend. The stippled regions represent the trends at/above 95%
 671 confident level. The colors present the climatological distributions of the monthly mean zonal \bar{q}_ϕ in
 672 four seasons.

673

Figures

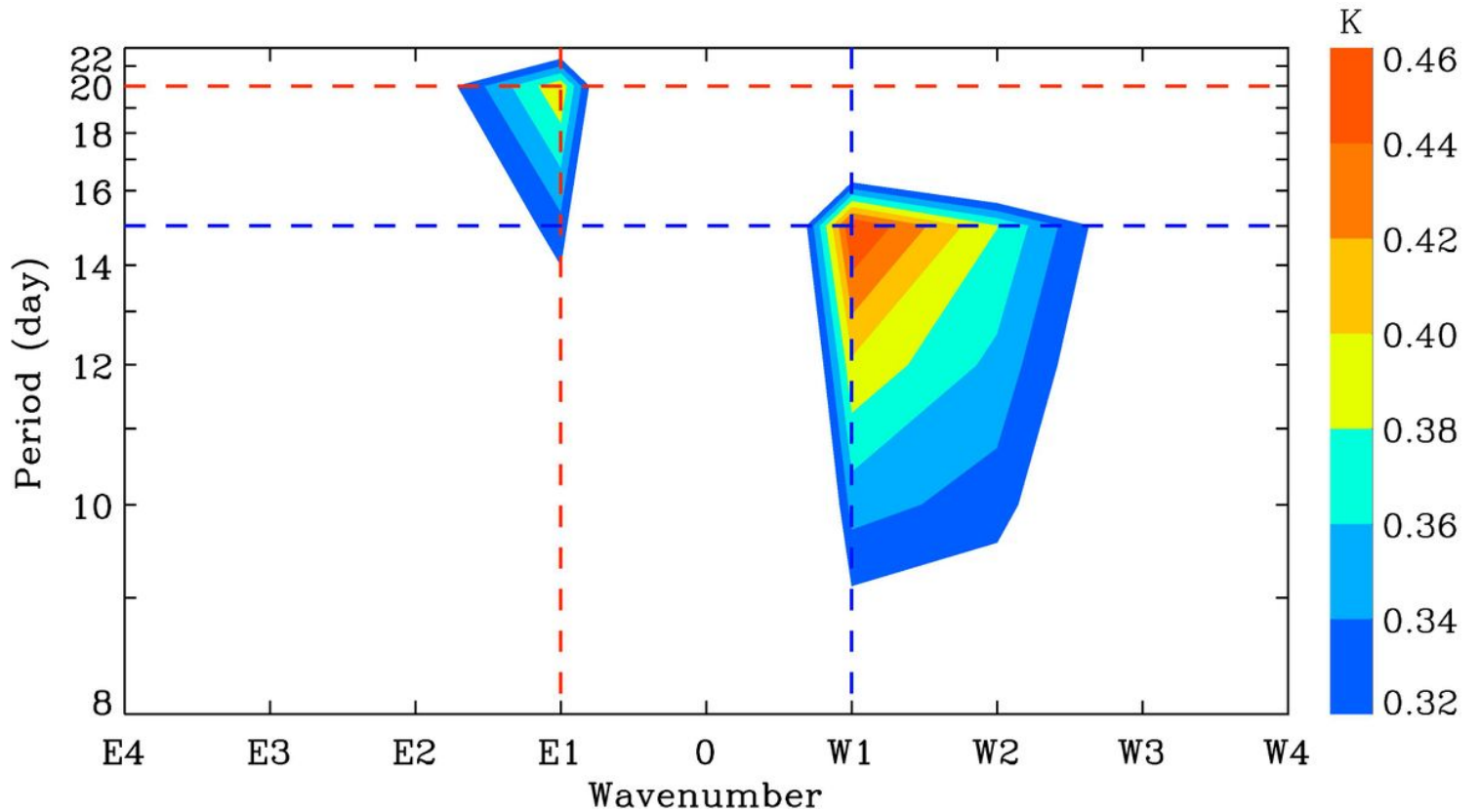


Figure 1

Mean frequency-wavenumber spectrum of temperature (in K) from February 1979 to January 2018 (39 years in total) at 37 pressure levels from 1000 hPa to 1 hPa. W (E) represents westward (eastward) propagation.

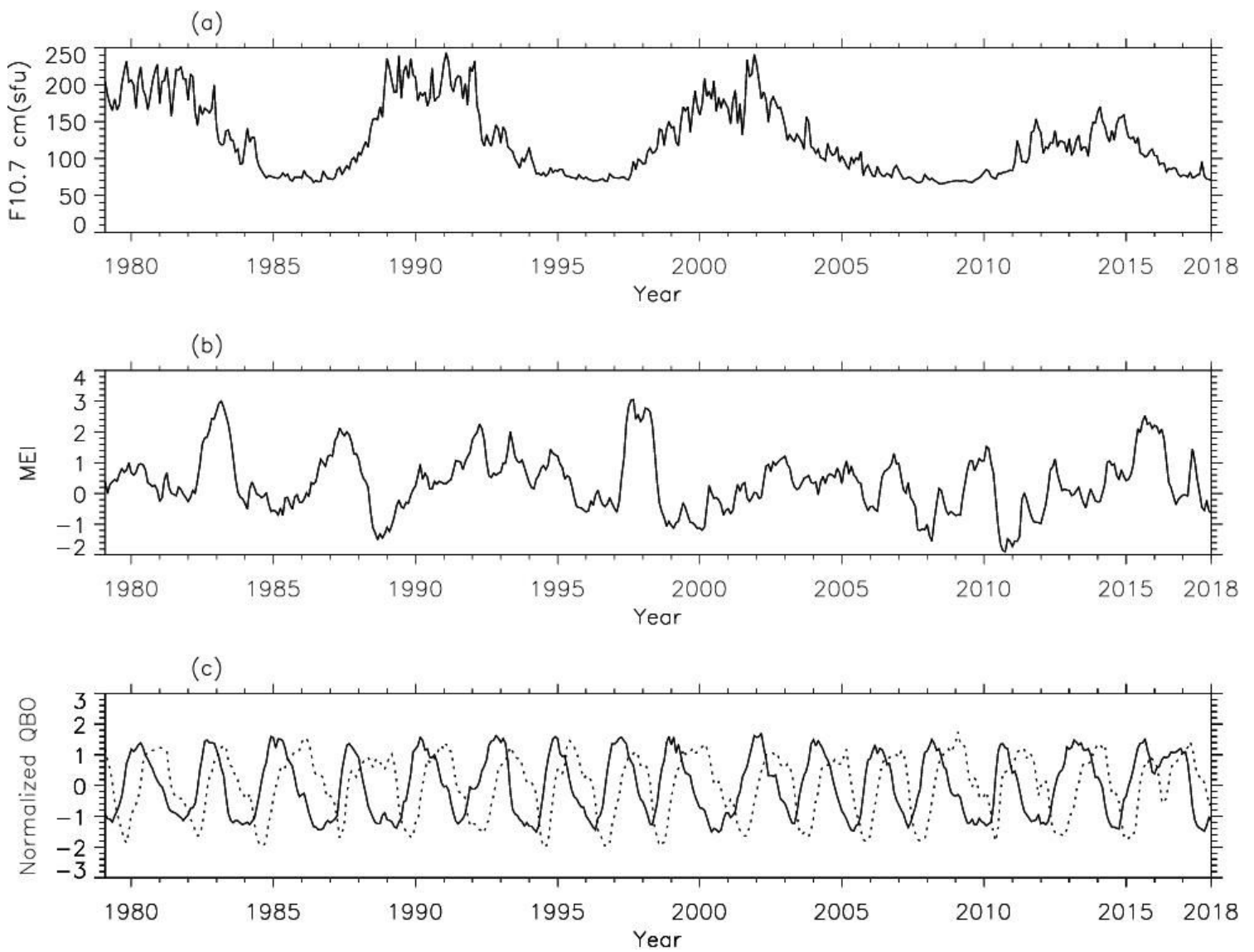


Figure 2

The time series of (a) SC index (F10.7cm flux), (b) multivariate ENSO index (MEI), and (c) the QBO indices on the monthly basis from February 1979 to January 2018, respectively.

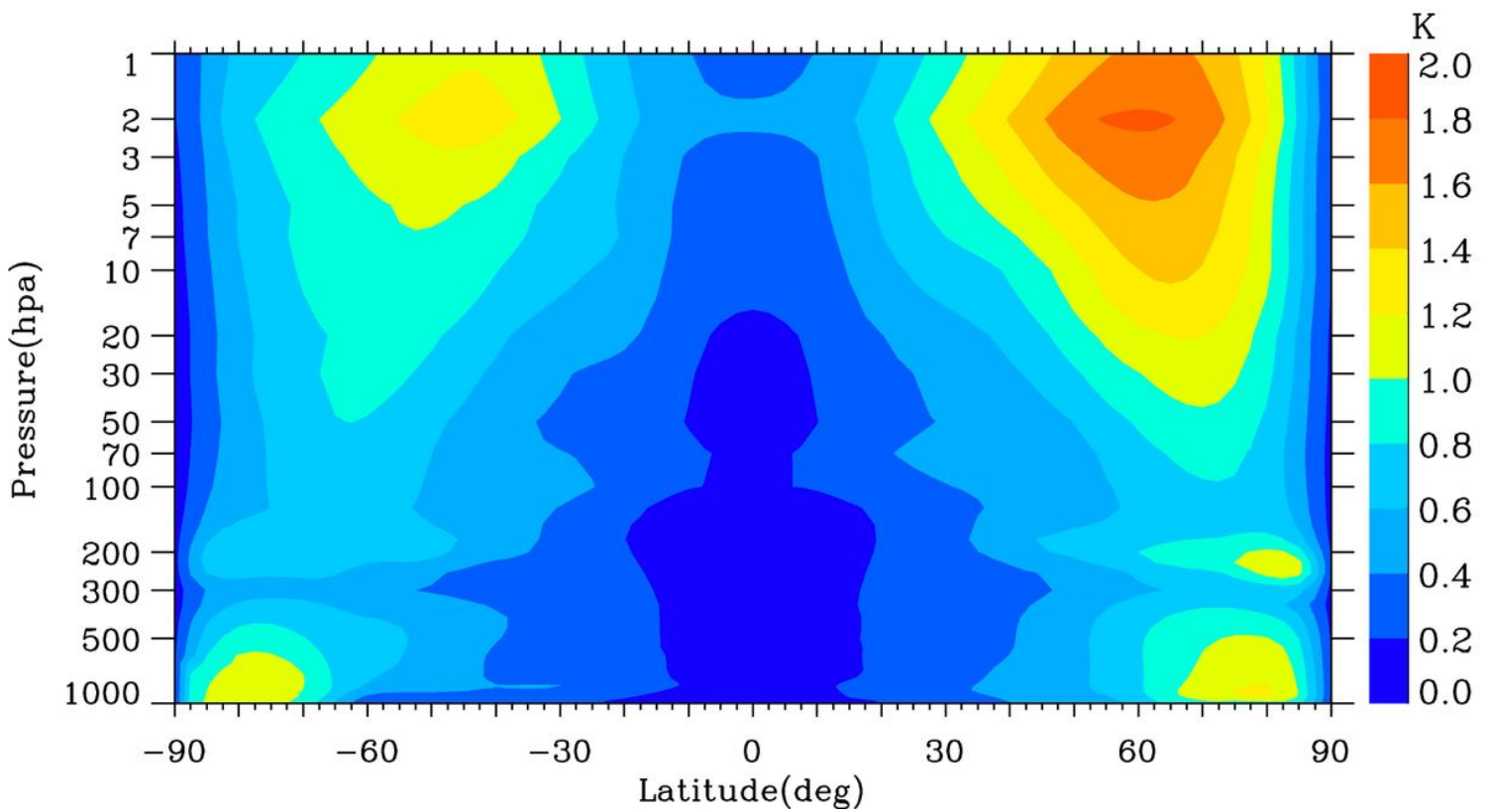


Figure 3

The latitude-pressure distribution of the monthly mean Q16W1 amplitude averaged over 39 years from the ERA-interim temperature data set.

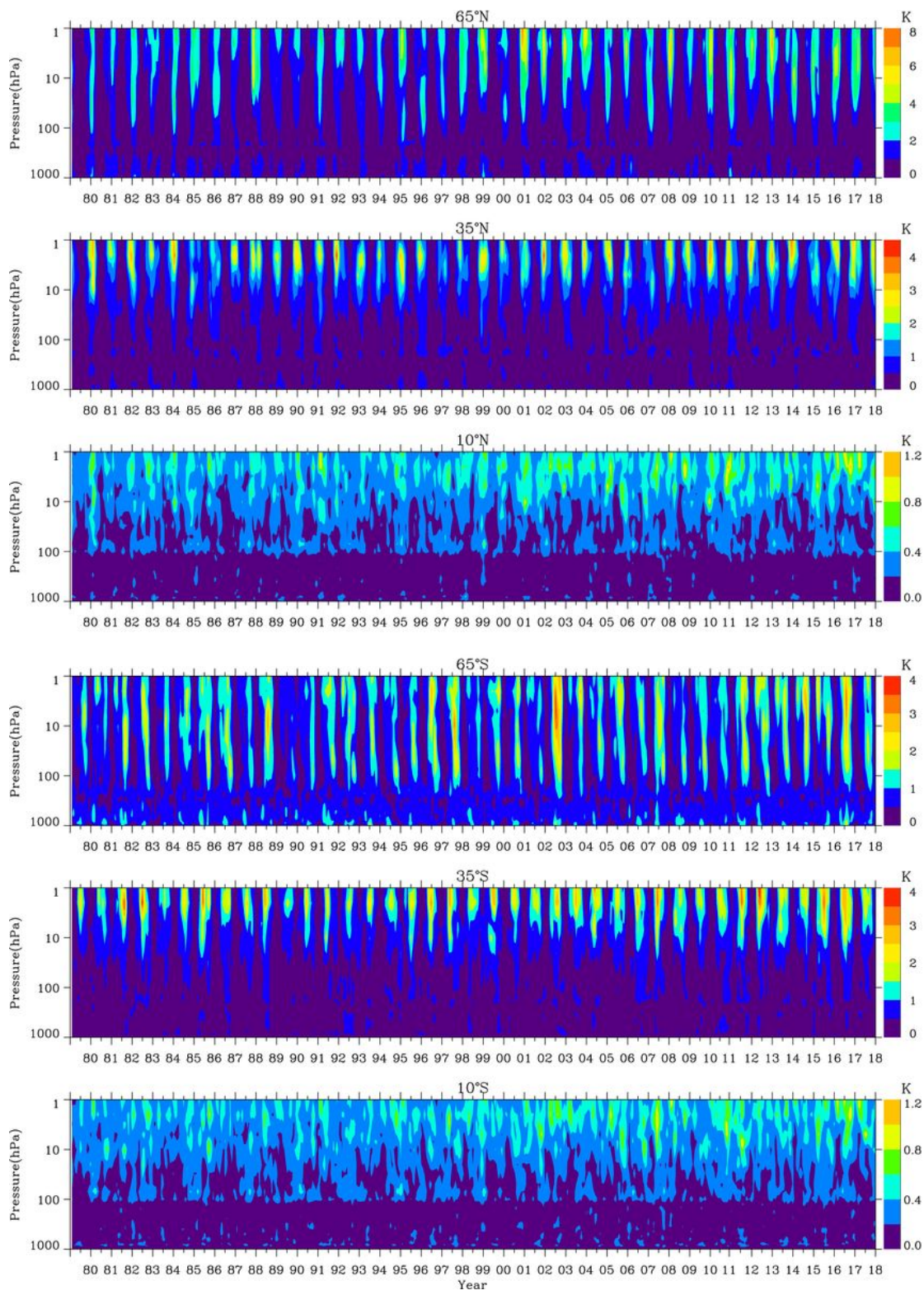


Figure 4

Month-latitude sections of the monthly and zonal-mean Q16W1 amplitude at high, middle, and low latitudes in the NH (three upper rows) and SH (three lower rows), respectively.

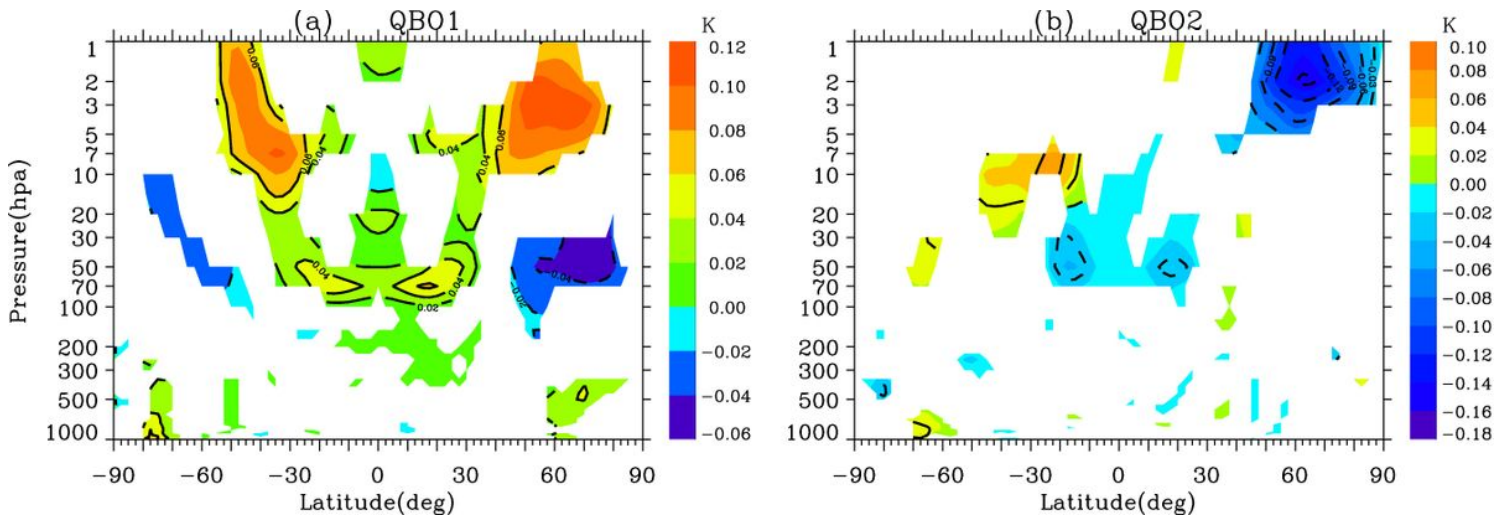


Figure 5

Latitude-pressure sections of the responses of the monthly-mean Q16W1 amplitude to (a) QBO1 and (b) QBO2, respectively. Only the results with the confidence level at/above 95% are plotted in contours. The solid and dashed contours denote the positive and negative responses, respectively.

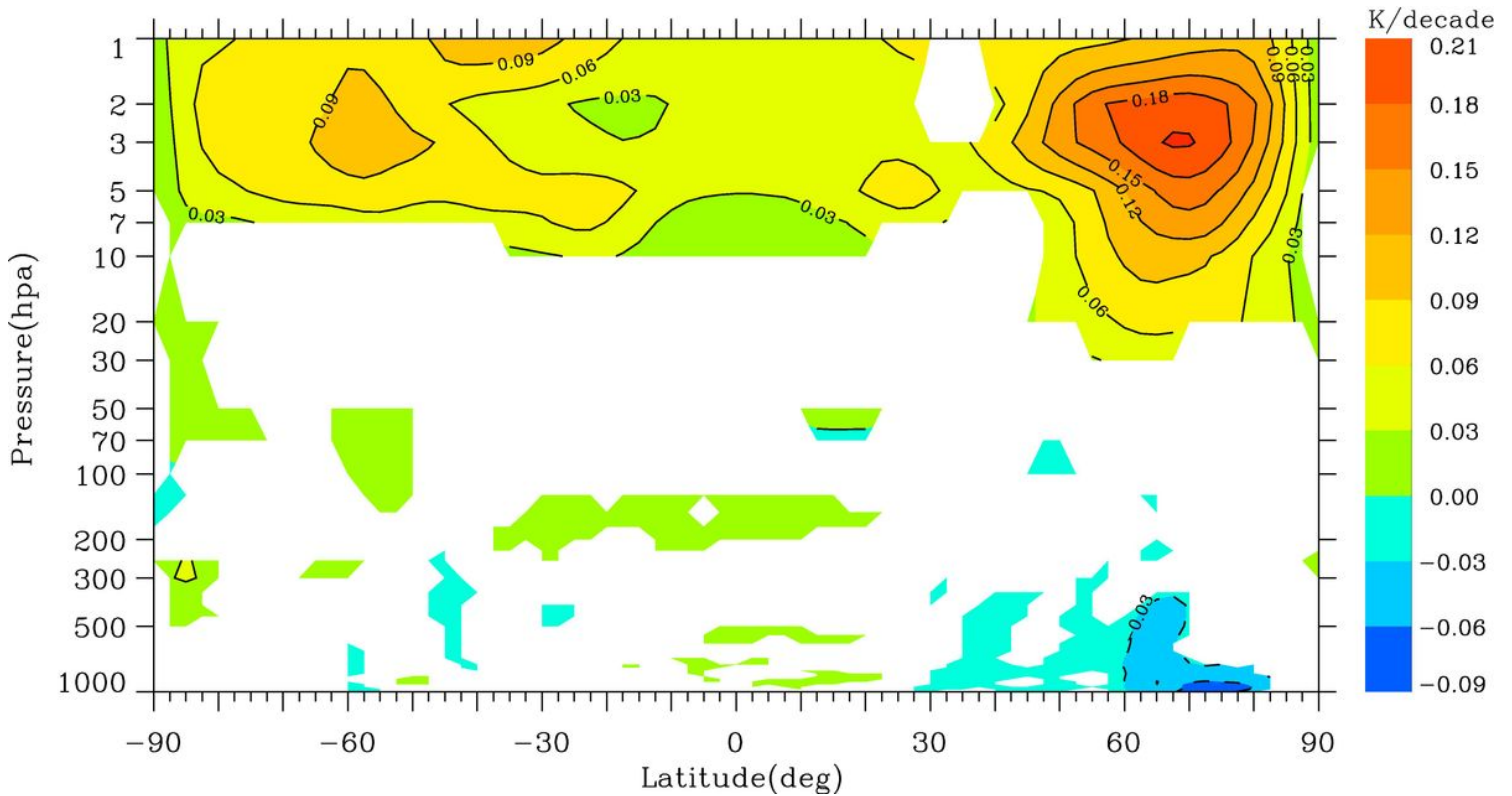


Figure 6

Long-term trend (in K per decade) as a function of pressure and latitude of the monthly mean Q16W1 amplitude obtained from the 39 years ERA-interim temperature data set. Only the results with the confidence level at/above 95% are plotted in contours. The solid and dashed contours denote the positive and negative trends, respectively.

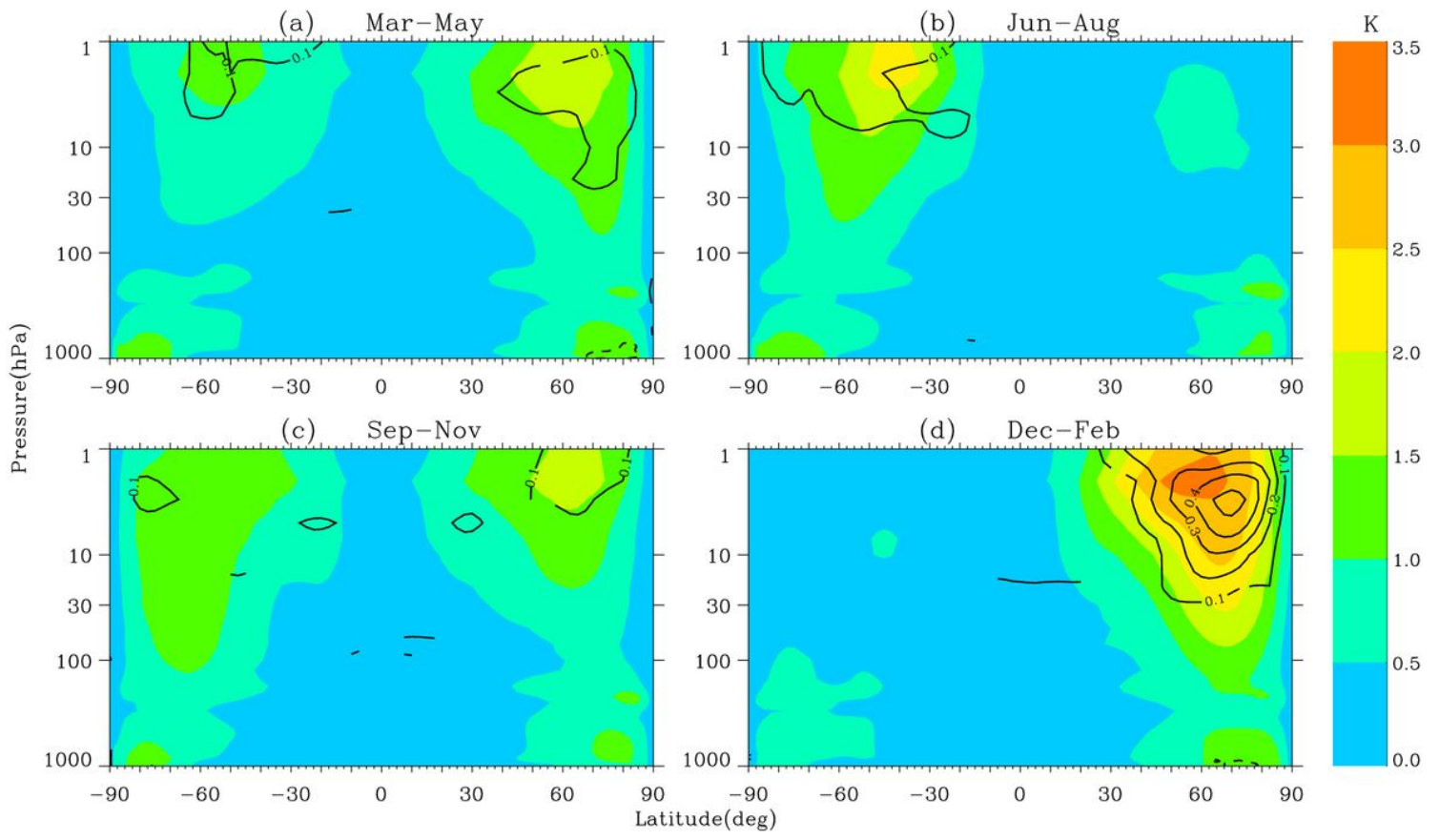


Figure 7

Seasonal variation of the Long-term trend (in K per decade) as a function of latitude and pressure of the monthly-mean Q16W1 amplitude from the 39 years ERA-interim temperature data set. The solid and dashed contours denote the positive and negative trends, respectively. The black contours denote the trend with confident level at/above 95%. The colors represents the climatological distributions of the monthly mean Q16W1 amplitude in four seasons.

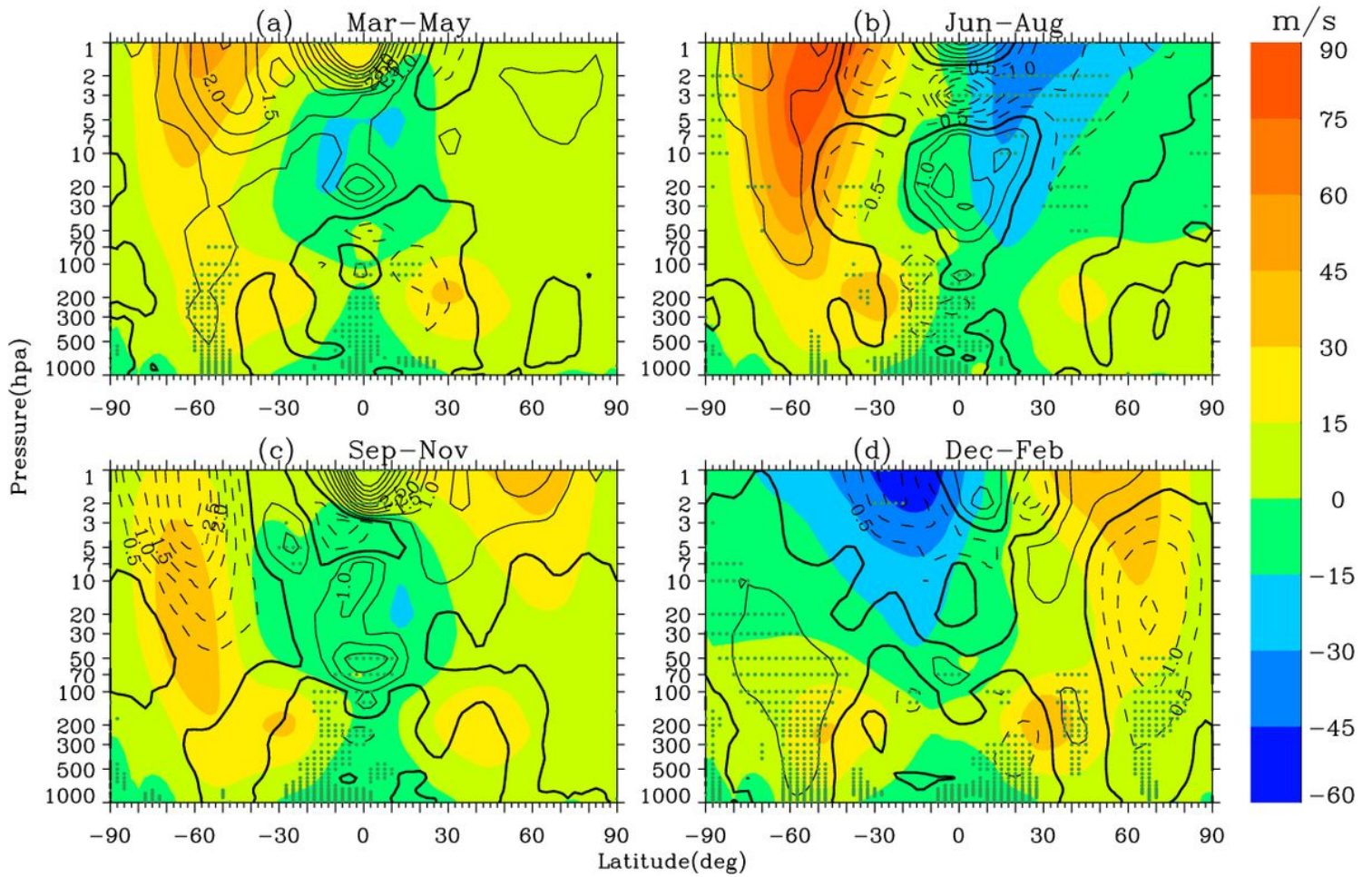


Figure 8

Trend (contours, units: m/s/decade) of the monthly mean zonal wind in four seasons derived from the 39 years ERA-interim zonal wind set. The solid and dashed contours denote the positive and negative trends, respectively. The thick black contour represents the 0 value. The stippled regions represent the trends at/above 95% confident level. The colors present the climatological distributions of the monthly mean zonal wind in four seasons.

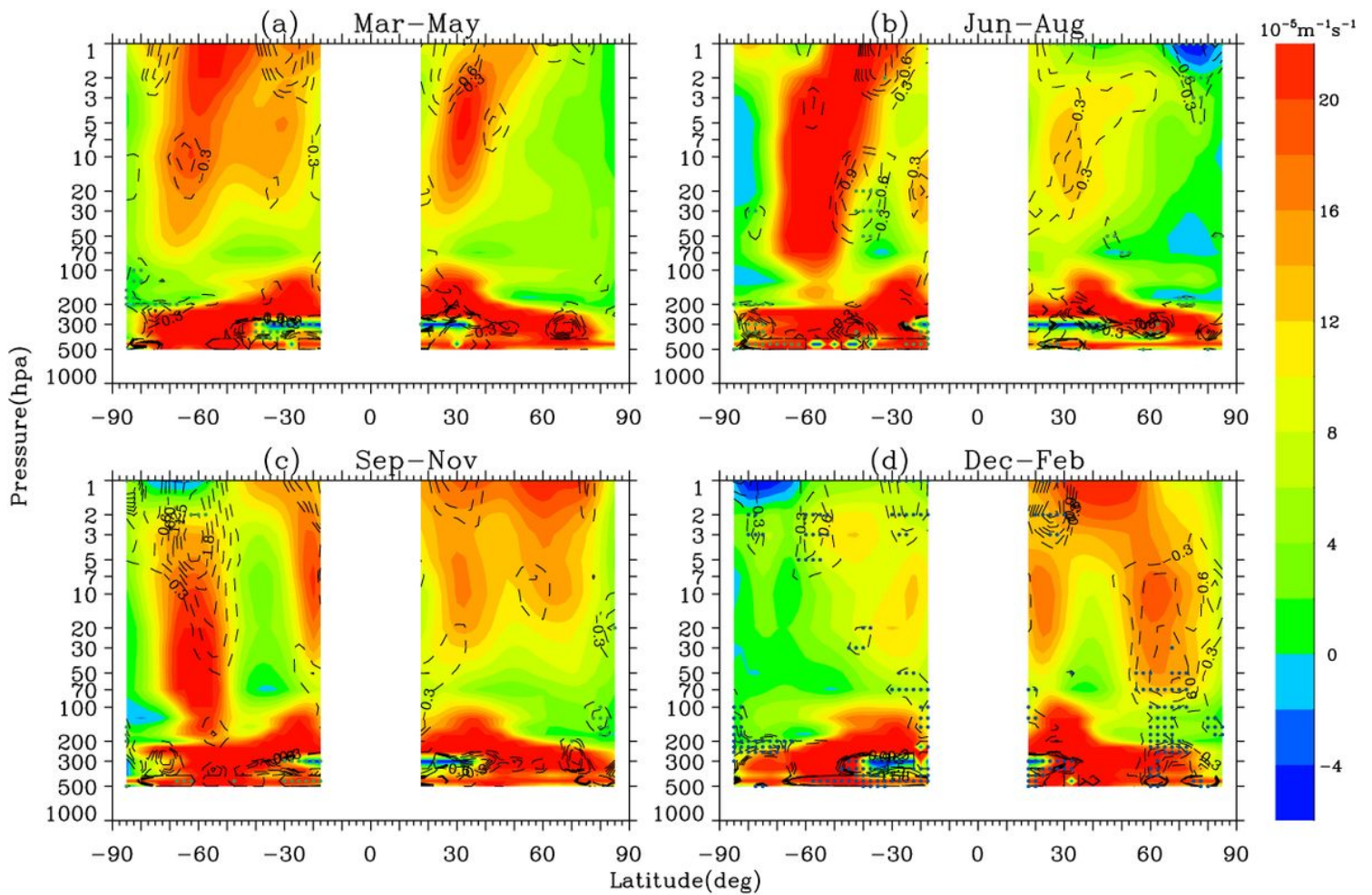


Figure 9

Trend (contours, units: $10^{-5} \text{ m}^{-1} \text{ s}^{-1}/\text{decade}$) of the monthly mean $q\Phi$ in four seasons. The dashed contours denote the negative trend. The stippled regions represent the trends at/above 95% confident level. The colors present the climatological distributions of the monthly mean zonal $q\Phi$ in four seasons.

Supplementary Files

This is a list of supplementary files associated with this preprint. Click to download.

- GraphicalAbstract.jpg